LA-12962-MS

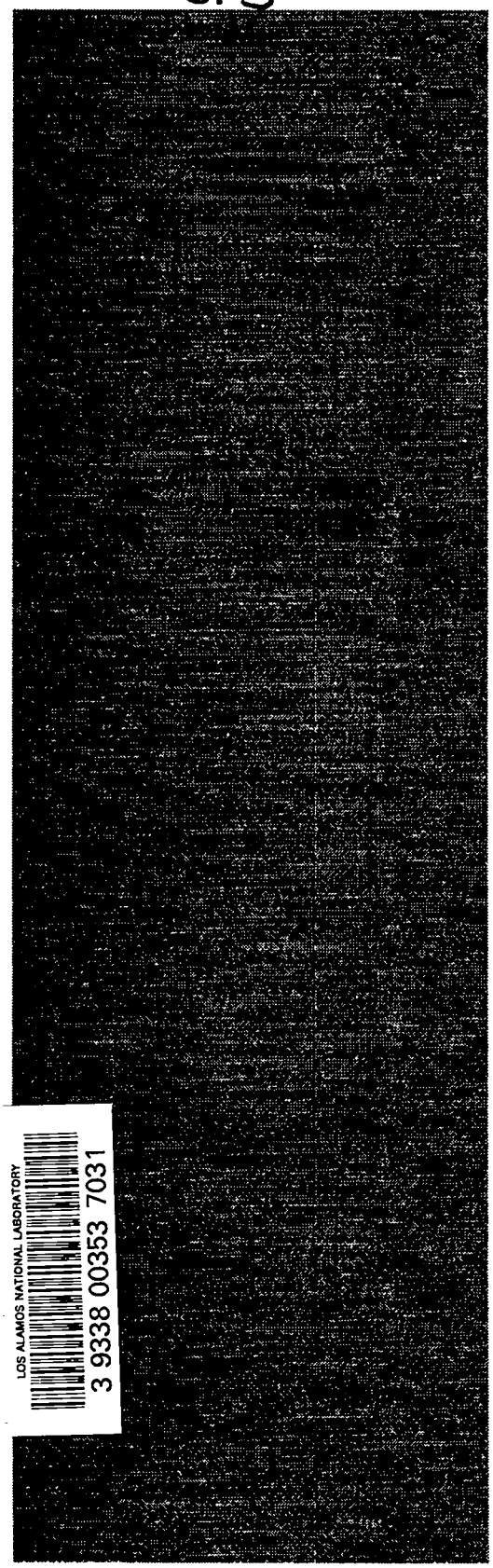

Atmospheric Transport of Neutrons and Gamma Rays from a High-Altitude Nuclear Detonation

Los Alamos
NATIONAL LABORATORY

Los Alamos National Laboratory is operated by the University of California for the United States Department of Energy under contract W-7405-ENG-36.

Edited by Martha Lee DeLanoy, Group CIC-1

This work was supported by the U.S. Department of Energy, Research and Technology Division, Office of Nonproliferation and National Security.

An Affirmative Action/Equal Opportunity Employer

LA-12962-MS

UC-700
Issued: July 1995

Atmospheric Transport of Neutrons and Gamma Rays from a High-Altitude Nuclear Detonation

R. C. Byrd

Los Alamos
NATIONAL LABORATORY
Los Alamos, New Mexico 87545

ATMOSPHERIC TRANSPORT OF NEUTRONS AND GAMMA RAYS FROM A HIGH-ALTITUDE NUCLEAR DETONATION

by

R. C. Byrd

ABSTRACT

Although the radiation outputs from nuclear detonations in free space are well established, few studies exist of the effect of atmospheric transport on the resulting intensity, energy, and time signatures. In this report we present calculations for generic sources located at high altitudes, 20–50 km above the Earth's surface, in an atmosphere whose density decreases almost exponentially with height. The sources are instantaneous time bursts with simple energy dependences: gamma rays use an evaporation spectrum; neutrons use either a Gaussian fusion or a Maxwell fission spectrum. The observation angles vary from vertical to 5° below the horizon, and detectors are placed in either geosynchronous or low Earth orbits (100 km). All calculations use the Monte Carlo N-Particle (MCNP) transport code in either its photon, neutron, or coupled neutron-photon modes, with the coupled mode being applied to the production of gamma rays by neutron inelastic scattering. The standard MCNP outputs are analyzed to extract the intensity, energy, and time dependences of the fluence as functions of either source altitude or observation angle. In general, the intensities drop rapidly below about 30-km source altitude or +5° slant angle. Above these limits, the gamma-ray signal loses substantial intensity but still contains most of the original source information. In contrast, neutron scattering produces little or no decrease in intensity, but it rapidly degrades much of the information about the original source spectrum. Finally, although there is abundant gamma-ray production from neutron inelastic scattering, the resulting signatures appear to provide little additional information.

---

1. INTRODUCTION: LAYOUT OF THE CALCULATIONS

Overview. This section describes some of the previous papers on atmospheric transport of nuclear radiation, discusses the assumptions that limit the present study, and summarizes the calculational approaches used. Much of the discussion concerns the setup of the MCNP input files, particularly (1) the geometrical relationships between the source and detector and (2) the variation of atmospheric density with altitude.

Previous Work. A cursory inquiry into previous atmospheric transport calculations provided several examples of earlier work. Most of the calculations were made by Rand

Corporation in the 1960s; they deal primarily with x-rays at energies below 100 keV or with specific neutron signatures. For x-rays, an excellent example is presented in the unclassified memorandum "Transport Calculations Pertinent to Satellite Detection of X-Rays from Near Earth Nuclear Explosions," by H. W. Hubbard (1969).[1] Related calculations at higher energies appear to have been made by Hubbard but were not published; in particular, we have located a set of figures labelled "Gamma Ray Transport Calculations."[2] These results were compared with those from the present study and found to be generally consistent. A more recent unclassified study was made at Los Alamos National Laboratory (LANL) and is summarized in "Simulation of Atmospheric Transmission," by E. Fenimore, C. Ho, and B. Smith (1992);[3] its results will be referenced as appropriate. For neutrons, previous calculations were usually directed at a particular problem, such as those in the classified memorandum "A Monte Carlo Calculation of the Neutron Time-Of-Flight Spectrum for the STARFISH Event (U)," [4] by J. I. Marcum (also of Rand Corporation). The most general neutron study appears to be that in the classified report "Atmospheric Neutron Leakage Spectrum from a Hypothetical Endoatmospheric Nuclear Detonation as Viewed from Space (U)," by G. Auchampaugh (1992),[5] which is the immediate predecessor to the present work. In particular, that reference includes calculations of the fast-neutron energy spectrum observed for detonations very deep into the atmosphere, although only for detectors located directly above the source.

Present Studies. The input source functions for the present work are intended to represent nuclear-weapon outputs only generically. Gamma rays have a simple evaporation spectrum, and neutrons use either a Maxwell fission distribution, a Gaussian d-T fission distribution, or a 1:1 combination of the two components. Both neutrons and gamma rays are transported, and coupled calculations are used to estimate the production of gamma rays from (n,n′) reactions. Our analyses are focused on a transition region around a 30-km source altitude. The results at higher altitudes approach the free-space values, and those much below this range change rapidly enough that few useful generalizations can be made. Because deep-penetration transport is not required, the setup for our MCNP calculations is relatively straightforward. The observation angles are measured relative to a horizontal plane through the source and vary from 90° (directly vertical) to just below the horizon (−5°). The detector locations are usually chosen to be geosynchronous orbits, although some results will be shown for a low (100-km) altitude. The radiation detectors themselves are unspecified, and their response will be discussed only in terms of very general capabilities.

MCNP Operation. The MCNP input file consists primarily of thin Earth-centered shells of constant atmospheric density that are divided into vertical cylinders centered about the source point. (See Ref. 5 for a complete specification.) For simplicity, separate calculations were used for each of the three transport modes (photon, neutron, and coupled), and separate runs were made for each of five source altitudes. Each run used 10^6 source particles and included tallies for two orbits (100 km and geosynchronous) at ten different slant angles. A few additional cases were used to obtain high-resolution time spectra. The accumulated tallies include only photons (for gamma-ray sources) and either neutrons or photons (for neutron sources). Energy cutoffs are imposed either naturally by the rising low-energy absorption in the atmosphere (for photons) or by the maximum time durations expected with reasonable detectors (for neutrons). Because deep-penetration transport was not required, the only variance-reduction techniques employed were MCNP ring-detector tallies. In this procedure, Monte Carlo transport is relied on to generate the proper spatial and temporal distributions of the particles around the source, and simple attenuations are used to estimate the probability that the scattered particles would reach a remote detector location. As long as the stochastic calculation adequately samples the source region, this procedure should be ideal for our case, where no interactions are expected near the detector. An additional feature of this approach is its provision for

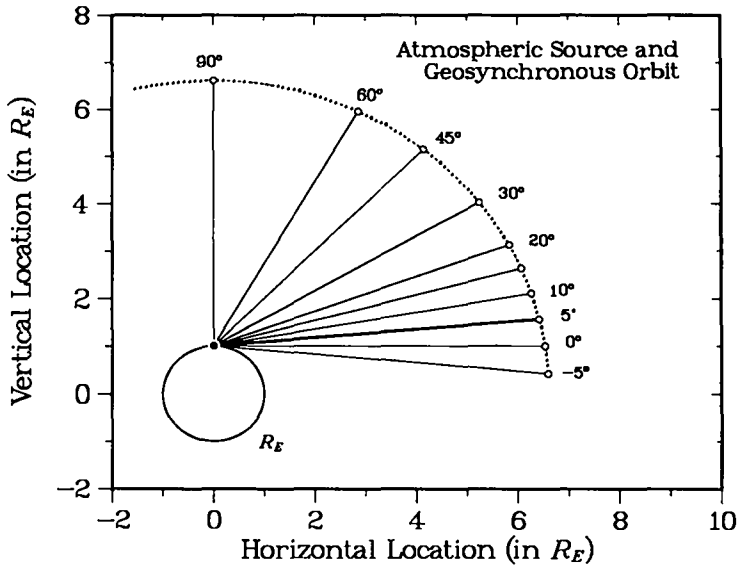

Fig. 1.1a. Scale illustration of the geometry used with the calculations for a source at 30 km and a detector in a geosynchronous orbit with slant angles between 90° (vertical) and −5° (below horizontal). The offset of the source from the Earth's center causes the source-to-detector distance to increase slightly toward lower slant angles.

separate total and uncollided (direct) contributions, which will be very useful in interpreting the results. From each run the output tallies were pairs of two-dimensional arrays of time-versus-energy bins, total and uncollided, with one pair for each combination of orbit and observation angle. These arrays were converted into the desired differential or integral quantities by postprocessing routines run external to the MCNP code.

Source and Detector Geometry. The large-scale layout of our problem is illustrated in **Fig. 1.1a**. For this case, the source is placed in the atmosphere (at a 30-km altitude), and the detectors are located in a geosynchronous orbit at R_g = 42 161 km (6.61 R_E). The complete set of source altitudes is 20, 25, 30, 35, and 50 km. The coordinates are related to the cartesian system used by MCNP, with the origin at the Earth's center and the z-axis vertical. The ten detector slant angles, measured relative to the Earth's horizon, are always 90°, 60°, 45°, 30°, 20°, 15°, 10°, 5°, 0°, and −5°. The narrower spacing at lower angles is explained by reference to **Fig. 1.1b**, which shows the paths through the atmosphere and the detector locations for a 100-km orbit. The path length in the atmosphere changes very slowly for vertical angles (near 90°), but it increases dramatically for slant angles near the horizon. For the last few angles, each 5° decrease almost doubles the path length. Note that this path-length change and the resulting scattering effects would be very similar in the geosynchronous case of Fig. 1.1a; the major difference there is the large, slowly changing flight path beyond the atmosphere. Finally, the detailed view in **Fig. 1.1c** uses an expanded vertical scale to show that the 0° and especially the −5° paths pass quite close to the Earth's surface. Because the +5° case represents the last angle before the path length increases rapidly, its results will usually be highlighted in the analyses below. The distortion in this figure also emphasizes the need to use a realistic spherical geometry, as opposed to the simple planar atmospheres employed by codes such as ONEDANT.

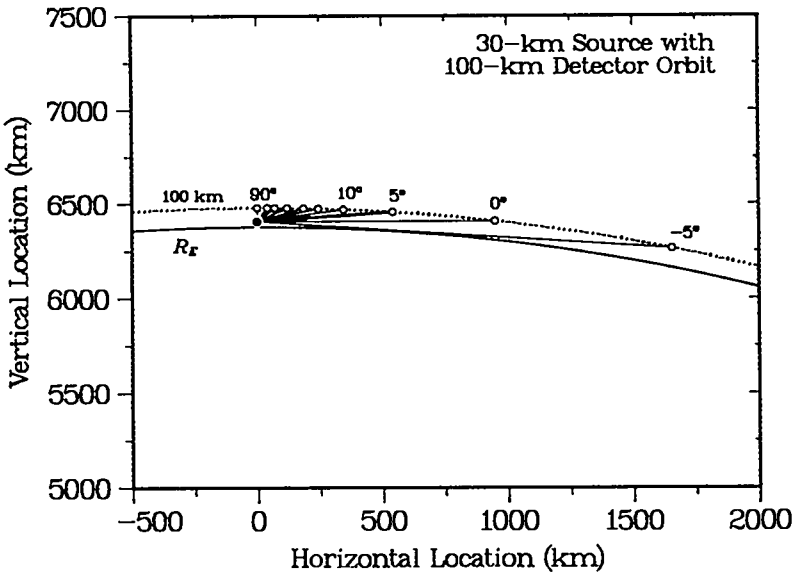

Fig. 1.1b. Enlarged geometry for the calculations, shown to scale to emphasize the path lengths through the atmosphere and the detector locations for a 100-km orbit. The paths change slowly for vertical angles, but they increase rapidly as the detector approaches the horizon.

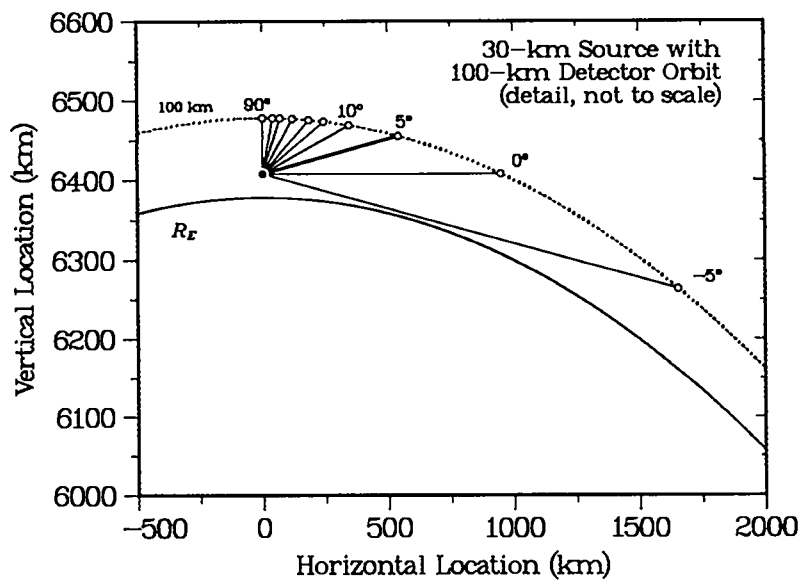

Fig. 1.1c. Geometry for the calculations, expanded vertically (that is, not to scale) to show the nearness to the Earth's surface for the paths at the two lowest slant angles.

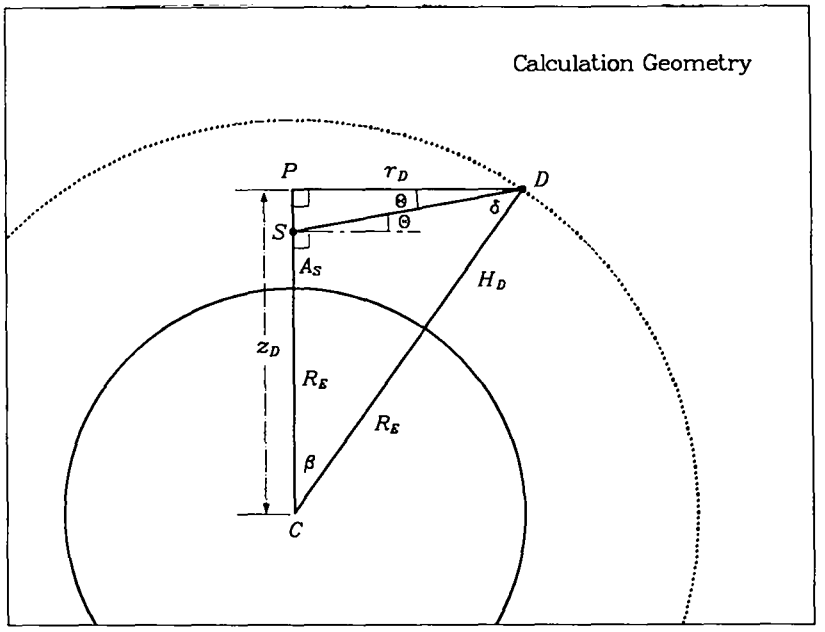

Fig. 1.2. Detailed geometrical relationships for the calculations (not to scale). The source altitude A_S, detector orbit H_D, and slant angle Θ are known quantities that must be converted into the MCNP tally parameters z_D and r_D.

MCNP Tally Geometry. To express the geometry of the source altitudes and detector angles in terms of the input parameters for the MCNP program, we use the relationships shown in **Fig. 1.2.** The source S is located along the z-axis at an altitude A_S above a spherical Earth of radius R_E. The detector D is assumed to be in a circular orbit at height H_D above the surface. The remaining independent parameter is Θ, the slant angle above the horizon as measured from the source. Because the problem is symmetric about the z-axis, the flux tallies can be obtained by placing an MCNP ring detector at the appropriate altitude z_D and radius r_D. For each source altitude A_S, multiple detector heights H_D and slant angles Θ can be tallied in a single MCNP run. The z_D and r_D values needed for the MCNP tallies are calculated as follows. From triangle CPD,

$$z_D = (H_D + R_E)\cos\beta$$

$$r_D = (H_D + R_E)\sin\beta \ .$$

From triangle CSD,

$$\frac{\sin(\pi/2 + \Theta)}{H_D + R_E} = \frac{\sin\delta}{A_S + R_E} \ ,$$

where the angles δ and β are related by

$$\beta + \frac{\pi}{2} + \Theta + \delta = \pi \ ,$$

and δ is obtained from

$$\delta = \tan^{-1}\left(\frac{(A_S + R_E)\sin(\pi/2 + \Theta)}{[(H_D + R_E)^2 - (A_S + R_E)^2 \sin^2(\pi/2 + \Theta)]^{1/2}} \right) \ ,$$

where an arctangent function is used for compatibility with standard FORTRAN coding.

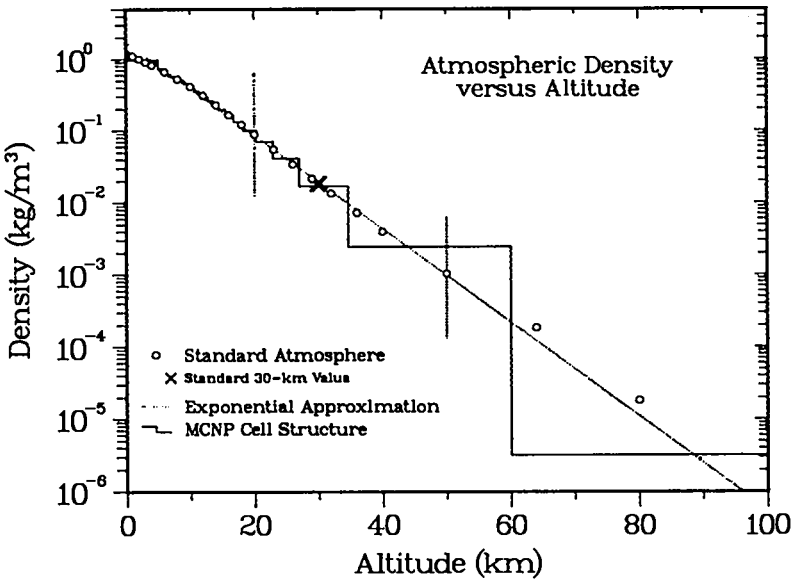

Fig. 1.3a. Altitude variation of the density for the standard (points), exponential (line), and MCNP (histogram) atmospheres. The vertical lines mark the 20- to 50-km range of source altitudes used for the present calculations.

Model Atmosphere. The altitude variation of the atmospheric density determines much of the scaling behavior of the transport problem, and this scaling is reflected in the layout of the MCNP input file. The atmosphere used for the calculations was taken directly from the previous calculations in Ref. 5. It has a uniform, altitude-independent composition of 79.1 parts nitrogen, 20.4 parts oxygen, and 0.48 parts argon. These values are similar to the standard composition given in Ref. 6, which is 78.08 N, 20.95 O, 0.93 Ar, and 0.034 parts trace elements. The density varies essentially exponentially with altitude. To illustrate, the open circles in **Fig. 1.3a** show a set of density values taken from the standard atmosphere of Ref. 6. These values are compared with the dotted line, which is an exponential density function $\rho(a) = \rho_0 \exp(-a/A_0)$. Here a is the variable altitude, and the constants $\rho_0 = 1.63$ kg/m^3 and $A_0 = 6.69$ km were chosen to reproduce the standard value at 30 km (the bold $\times$ symbol in the figure). The deviations from the exponential function near the Earth's surface and at high altitudes are primarily temperature effects. Our calculations cover the range of source altitudes between the two vertical lines. The histogram shows the discontinuous density structure used in MCNP, which was taken from Ref. 5. The dimensions of this structure were chosen to be comparable to the mean free paths for neutrons and gamma rays at our reference 30-km source altitude, which are 6-9 km (10–15 g/cm^2). Integrating the exponential density function gives a cumulative depth function $T(a) = T_0 \exp(-a/A_0)$, with $T_0 = \rho_0 A_0 = 1089$ g/cm^2. **Figure 1.3b** compares this function with summations over the standard atmosphere and the tabulated values from Ref. 5, which give total thicknesses (at the Earth's surface) of 1032–1035 g/cm^2. This integrated depth function $T(a)$ is important for calculating the attenuation through the atmosphere, while accurate differential densities $\rho(a)$ are needed to represent the effects of scattering at different altitudes. To satisfy these requirements, the standard densities from Ref. 6 (not the exponential approximations) were converted[5] into the MCNP cell densities in a way that preserves the integrated density. In retrospect, for the present work it would

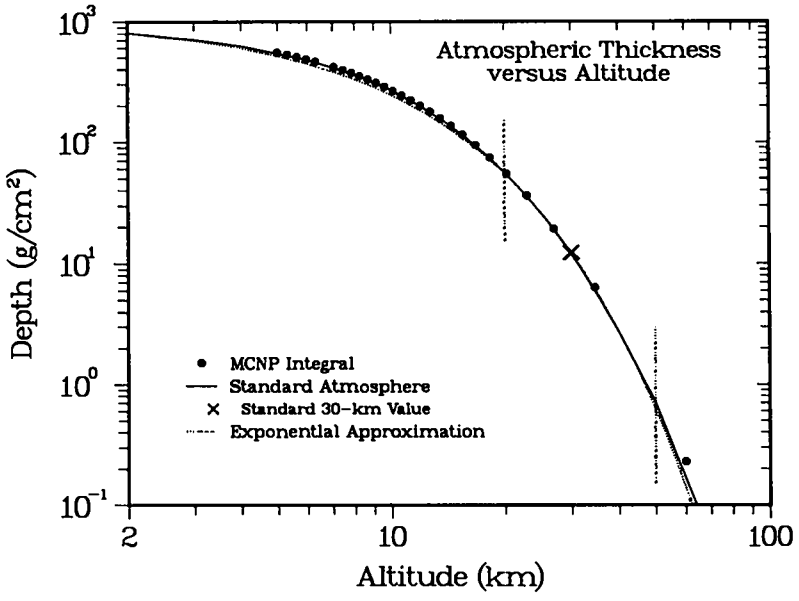

Fig. 1.3b. Transmission as in Fig. 1.3a, but for the integrated density dependence of the previous (Ref. 5), standard (Ref. 6), and exponential atmospheres.

have been better to revise the MCNP geometry of Ref. 5 by more finely subdividing the high-altitude cells to reduce the size of the density discontinuities. It is likely that the existing coarse structure introduces slight irregularities at certain combinations of slant angle and source altitude.

Summary. The present calculations of atmospheric transport give results that are comparable with those from earlier, more limited studies. Because our emphasis is on the effects of radiation transport, not on specific performance capabilities, we have used generic source functions and schematic detectors. In all cases, the calculations use source altitudes of 20, 25, 30, 35, and 50 km and slant angles of 90°, 60°, 45°, 30°, 20°, 15°, 10°, 5°, 0°, and −5°. The MCNP input assumes a near-exponential atmospheric density and tallies the transported neutron and gamma-ray fluences by using simple ring detectors. External programs are used to convert the fluence per time-and-energy bin into the desired differential and integral quantities and to examine any correlations. The most important comments are as follows: (1) Our focus will be on source altitudes of 20–50 km, a range that is above 95–99% of the atmosphere; (2) the path length through the atmosphere, and hence the effect of scattering, changes rapidly at slant angles near the horizon.

Contents of the Report. This section has described the basis for the present calculational study. Section 2 continues with the calculations for gamma-ray sources; Section 3 covers the neutron signatures produced by fusion, fission, and fission-plus-fusion sources. Section 4 uses the same two neutron sources, but the output tallies are the gamma-ray fluences produced by (n,n′) inelastic scattering. Section 5 presents a summary and discusses the expected course of further work.

2. GAMMA-RAY SOURCE CALCULATIONS

Overview. We open our discussion with the simplest problem, the transport of gamma rays from an atmospheric source to a detector in either a geosynchronous or low Earth orbit. The original MCNP tallies are given in counts per energy-and-time bin; differential distributions are constructed off line by dividing through by the appropriate bin width. The first analyses concern the integral observables, where the tallied fluences have been summed over both energy and time. The results establish the overall behavior of the transported photons as functions of slant angle and source altitude. The only complication, which is unique to the photon case, is the need to express the results as either particle or energy fluences, each of which is useful for different aspects of the problem. Because typical photon detectors respond primarily to energy fluences, all our spectral distributions are energy-weighted. These distributions establish the detailed behavior of the fluence, which leads to a physical interpretation in terms of the connection between uncollided gamma rays and higher photon energies, versus the connection between scattered gamma rays and lower photon energies. This model is important because of two competing issues in photon transport. On one hand, photons at higher energies are shifted to lower energies by scattering, but photons at lower energies are strongly absorbed because of the rising interaction probability. It is difficult to predict the net result of these two effects without explicit calculations.

Integrated Photon Fluences. Our first analyses involve photon transport to a detector located in a geosynchronous orbit, with the results integrated over both time and energy. One view of the resulting fluence is given in **Fig. 2.1a**. The integrated particle fluences have been converted to effective transmissions by correcting for the solid angle at each slant angle. The dashed line segments show the direct, uncollided values; the solid curves are the total (collided plus uncollided) results. The light dotted line indicates 100% transmission, that is, the value obtained for transport in free space. For the direct fluence (dashed lines), this line is the upper limit; attenuation to lower values is caused by any photon interaction, no matter how slight its effect. In contrast, the total transmission (solid curves) counts any photon that reaches the detector, no matter what its final energy or arrival time. Thus, the total transmission can (and does) exceed the free-space limit because inscattering from the atmosphere near the source can be larger than the losses to direct attenuation. As should be expected, the total transmission varies more slowly than the direct value, which falls off rapidly at low source altitudes or slant angles (that is, longer paths). For example, Fig. 1.1c showed that direct transmission at $-5°$ is essentially impossible (and none is observed), but Fig. 2.1a indicates that scattering allows some photons to follow a path upward through the atmosphere and then across to the detector, giving a nonzero total transmission at this angle. Finally, in most of our figures the results for the borderline case will be emphasized by using darker lines and plotting symbols, as for the 30-km case shown here. This emphasis also makes it easier to identify a particular calculation by counting up or down from the reference case.

Energy Transmissions. Because the particle transmissions in Fig. 2.1a do not account for the energy losses in photon scattering, in **Fig. 2.1b** we show the corresponding energy transmissions. These values were calculated by dividing the transmitted energy fluence by the free-space values; a few of the total results are still greater than 1.0. The direct energy transmissions are slightly greater than the corresponding particle values, because the increased photon absorption at lower energies leads to preferential transmission of photons at higher energies. In contrast, the total energy fluences are lower than the particle values, because scattered photons that have lost part of their original energy can still reach the detector.

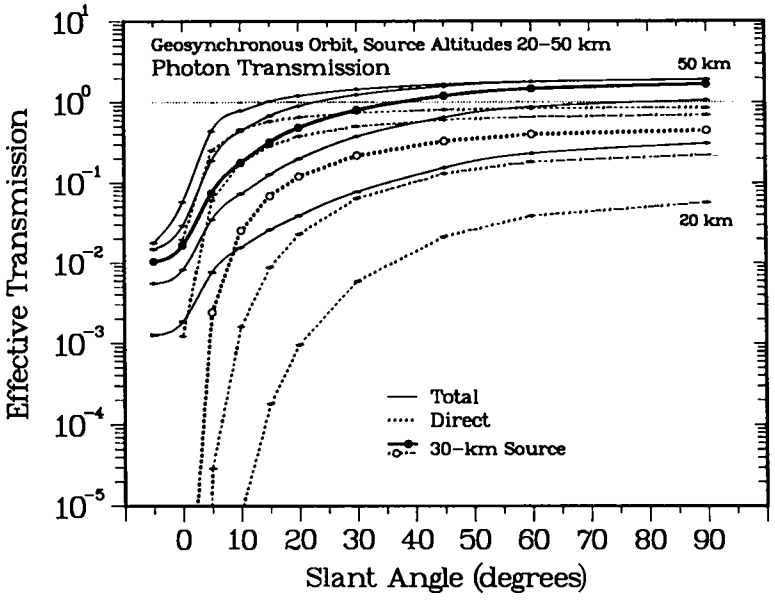

Fig. 2.1a. Angular dependence of the direct and total photon fluences for sources at different altitudes, after integration over both energy and time, as observed from a geosynchronous orbit.

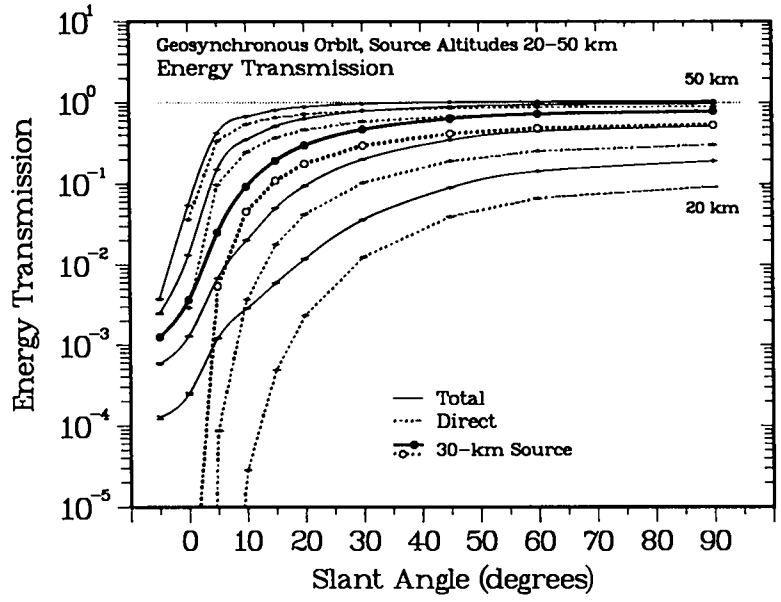

Fig. 2.1b. Angular dependence of the energy transmissions (direct and total) for sources at different altitudes, after dividing by the free-space values to obtain a relative value.

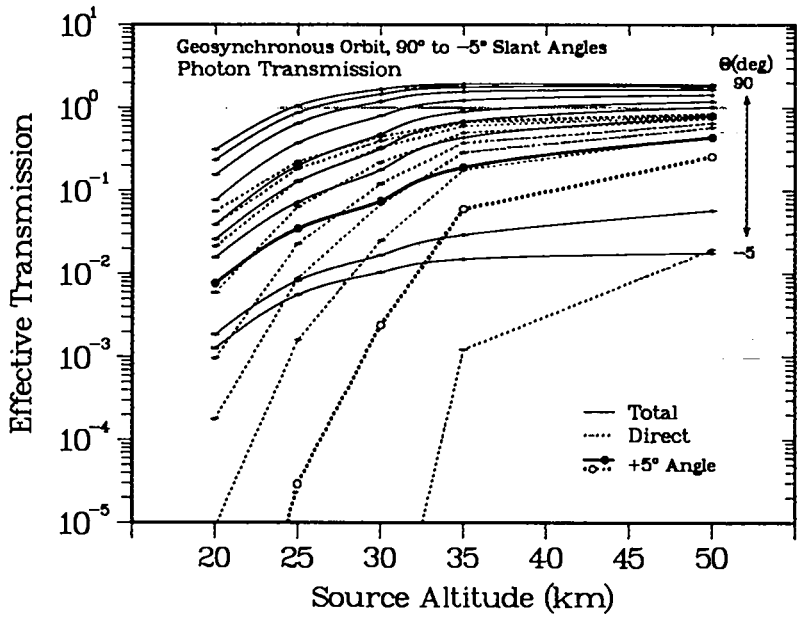

Fig. 2.1c. Transmissions as in Fig. 2.1c, but for the altitude dependence of the integrated photon fluences at different slant angles.

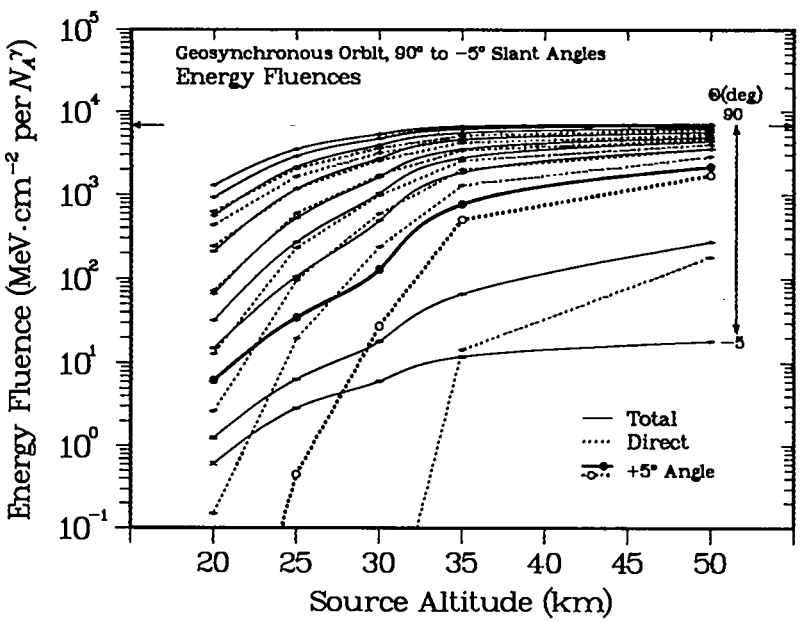

Fig. 2.1d. Transmissions as in Fig. 2.1b, but for the altitude dependence of the integrated energy fluences at different slant angles.

Altitude Dependence. The integrated gamma-ray fluences in Figs. 2.1a,b are plotted as functions of source altitude in **Figs. 2.1c,d**. To allow comparisons in terms of absolute magnitudes, the energy fluences in Fig. 2.1d are normalized to one mole of source photons (N_A^γ) but are not converted to relative transmissions. For reference, the two small arrows indicate the free-space value at 90°. As expected from the geometry of Fig. 1.1b, the falloff in the fluences at lower source altitudes is more gradual than the decrease with slant angle, although the cutoff in direct transport becomes quite steep for angles below +5° and altitudes below 30 km. Again, heavy lines and plotting symbols are used to indicate the borderline cases. The inflection near 30–35 km is possibly an effect of the discontinuous MCNP density variation from cell to cell. In general, however, our examination of the integrated results, whether as photon transmissions or as energy fluences, yields the same conclusions: At higher source altitudes and slant angles, that is, above 30 km or +5°, the intensity variations are gradual; below these limits, both fluences drop rapidly, especially in their direct, unscattered components.

Comparison with Previous Calculations. The angle dependence of the direct and total energy transmissions shown in Fig. 2.1b can be compared with the corresponding quantities from Figs. 4 and 5 of Ref. 3. The results are not expected to be precisely equivalent, because our calculations use a standard MCNP evaporation source, that is, $dN/dE = E\,\exp(-E/E_0)$, while Ref. 3 uses a simple exponential. In general, the agreement improves at higher source altitudes or at slant angles near the horizon. For the direct transmissions, our results at 30 km and 20 km are higher by factors of 3 and 5, respectively. The agreement is somewhat better for the total values, within a factor of 2 at 20 km and within 50% at 30 km. Given our greater mean energy, which increases the transmissions, the agreement is entirely reasonable in view of the large range of the transmission values.

Differential Energy Distributions for a 30-km Source. The more gradual falloff in the total fluences (scattered plus direct) in Figs. 2.1a–d suggests that additional detection sensitivity could be obtained if more of the scattered photon fluence were usable. To investigate this possibility, as well as to provide insight into the scattering mechanism, in **Fig. 2.2a** we show the energy characteristics of the gamma-ray pulse as it arrives at the detector. For this figure, the original MCNP tally in each energy bin (given in photons/cm^2 per source photon) has been multiplied by the bin's geometric centroid energy, divided by the bin's energy width ΔE, and normalized to one mole (N_A^γ) of source photons. This procedure provides the differential energy fluence $\Phi_E = E \times dN/dE$ in MeV·cm^{-2}·MeV^{-1} per N_A^γ, that is, differential probability in cm^{-2} per N_A^γ. As in the integral case, the energy weighting is included because typical photon detectors respond to energy fluences, not individual photon counts. Again, the solid lines show the total fluence, and the dashed lines show the direct, uncollided values. For reference, the single dotted line shows the free-space distribution at 90°; the corresponding distributions for other slant angles would be lower by at most 35%. The behavior of the scattered and direct components emerges clearly, with the direct fluences dominating the high energies and the scattered contributions being shifted to lower energies. The fluence at very low energies (below 25 keV) is strongly attenuated by the atmosphere at all slant angles, even for the most vertical paths. When combined with the integral results in Figs. 2.1a and 2.1b, Fig. 2.2a suggests that as the scattering increases, the lowest-energy photons are absorbed first, then the higher-energy photons are degraded in energy and eventually also lost.

Differential Time Distributions for a 30-km Source. Another view of the photon energy fluences is obtained by projecting the MCNP tallies onto the time axis. For **Fig. 2.2b**, we calculated the energy-weighted gamma-ray flux $\Phi_t = E \times dN/dt$ by multiplying the original MCNP tallies by each bin's centroid energy, summing over energy, dividing by the bin's time width Δt in milliseconds (ms), and then normalizing to one mole of source photons. The open circles show the direct component, which arrives at

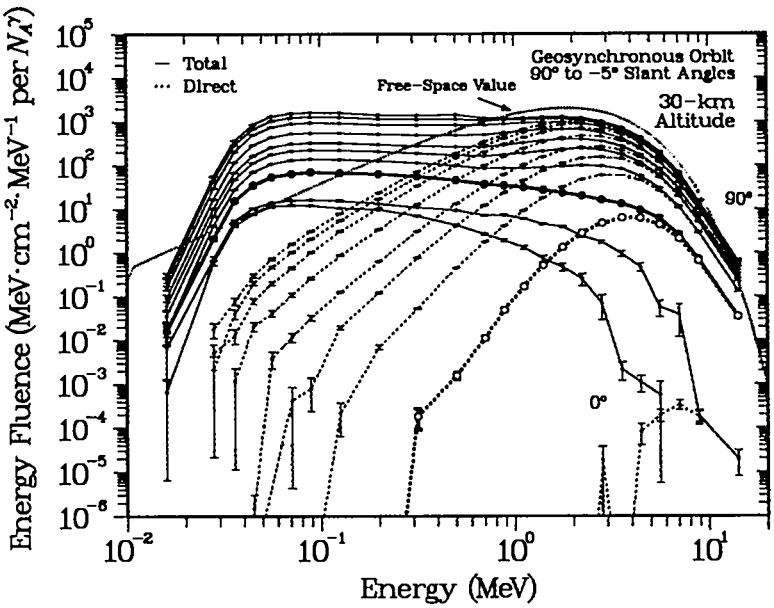

Fig. 2.2a. Energy dependence of the energy-weighted fluence from a source at 30 km incident on a detector in a geosynchronous orbit, normalized to one mole of source photons.

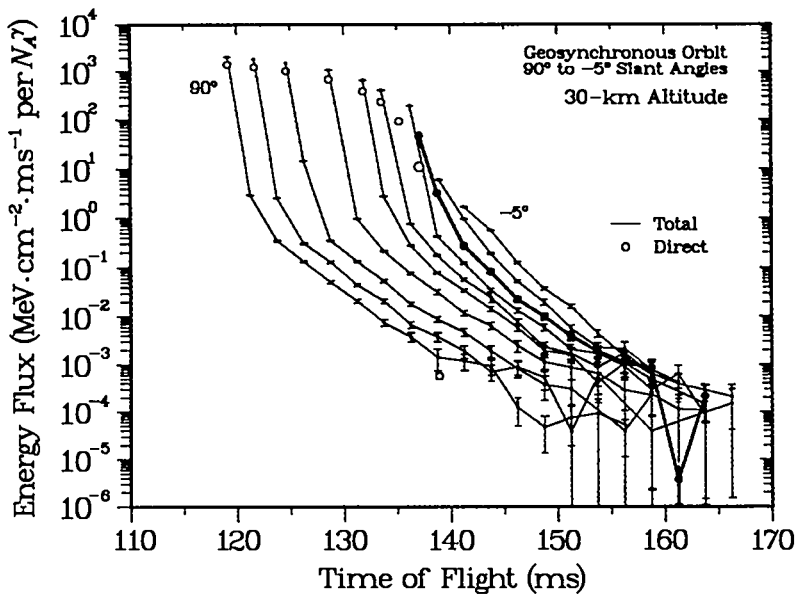

Fig. 2.2b. Time dependence of the gamma-ray energy flux from a source at 30 km incident on a detector in a geosynchronous orbit, normalized to one mole of source photons.

the detector in an instantaneous burst. The shift in propagation time from 120 to 140 ms is caused by the 18% increase in flight path between the 90° and −5° slant angles (see Fig. 1.1a). The solid lines show the total energy flux, which is dominated by the direct component at early times. The subsequent scattered flux immediately falls off by 2–3 orders of magnitude and then drops by another 4 orders of magnitude over the next 20–40 ms, which corresponds to an exponential time constant of about 2 ms. Because only the direct flux reliably reflects the source characteristics, at this 30-km source altitude the most useful results are expected for slant angles of +5° and above. The falloff below this angle is very rapid, as shown by the large difference between the direct points at +5° and 0°; no direct component is observed at −5°.

Angle Dependence for 20-km and 50-km Energy Fluences. The qualitative behavior of the 30-km distributions in Figs. 2.2a,b carries over smoothly to those at 20 km (**Fig. 2.3a**) and 50 km (**Fig. 2.3b**). The difference between the direct and total fluences in these figures emphasizes the changes caused by different source altitudes. At 20 km, the direct flux dominates only for slant angles above 45°; for 50 km, this dominance persists for all angles down to +5°. The importance of the limits on both source altitude (30 km) and slant angle (+5°) is seen clearly in the 20-km results, where the direct fluences are significant only at the highest angles.

Altitude Dependence for 90° and +5° Energy Fluences. Corresponding to the 20-km and 50-km results in Figs. 2.3a,b, in **Figs. 2.4a,b** we show the results for all source altitudes at the two extremes of the useful angular range, 90° and +5°. In the 90° case (Fig. 2.4a), the nearly identical total fluences above 25 km suggest that the atmospheric effects at these slant angles are restricted to absorption at the very lowest energies. The gradual decrease in the direct fluences indicates that many of these photons scatter without being absorbed or even substantially reduced in energy. This behavior contrasts with that at +5° (Fig. 2.4b), which suggests a rapid loss of direct fluence and a downscattering in energy at source altitudes below 35 km. At low source altitudes (Fig. 2.3a) or slant angles (Fig. 2.4b), the asymmetric shapes of the total spectra suggest that the ratio between the observed fluences at 100 keV and 2 MeV may be a useful indicator of the altitude of the original source.

Time Spectra at 90° and +5° versus Altitude. The large altitude variation in the energy spectra in Figs. 2.4a,b contrasts with the lack of variation in the corresponding time spectra. **Figures 2.4c,d** show the 90° and +5° cases. The 90° spectra are all essentially identical in shape; there is a rapid drop in intensity and then a gradual falloff of 3–4 decades over the next 20–30 ms. Although the initial drop is much less obvious at the +5° slant angle, the subsequent decay is almost the same. This behavior suggests that the scattered energy flux represents a secondary source whose behavior depends primarily on atmospheric transport, not on source characteristics. If valid, this characteristic time dependence may be a useful signature of a detonation in or near the atmosphere, as opposed to one in free space.

Early Time Behavior. Questions about the rapid falloff in intensity at the shortest times can be answered by additional calculations that examine the photon flux in this interval. First, **Fig. 2.5a** shows differential time spectra for three slant angles over the time range from 0–32 μs. For clarity, the time offsets for differences in propagation distance have been subtracted, so $t = 0$ represents the arrival time at the detector. On this time scale, the difference between the 90° and +5° angles appears to be one of magnitude, not shape, and in both cases the direct and scattered components are clearly separated. This two-component identification is apparently valid at all slant angles down to 0°. Continuing to even shorter times, in **Fig. 2.5b** we show the time-dependent integral of the +5° flux over the time range from 0–1200 ns. This integral presentation mimics the slow time

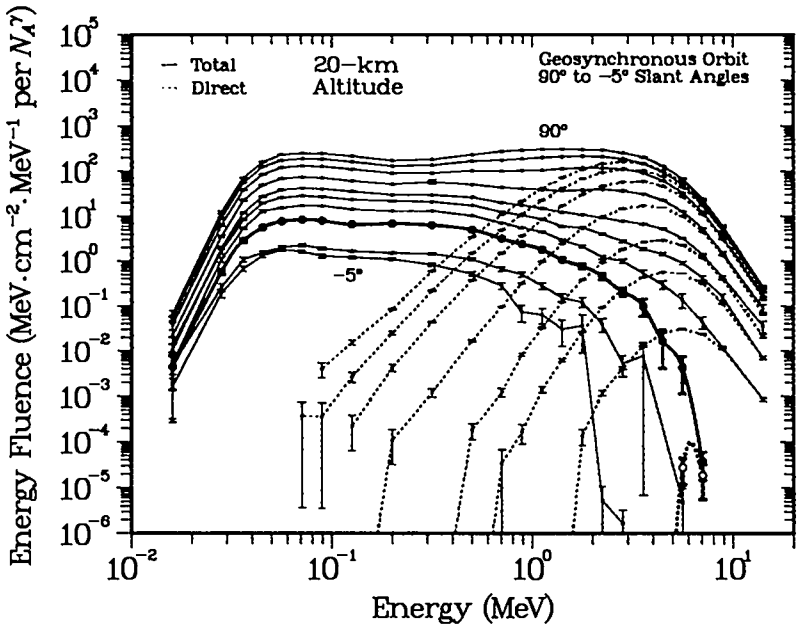

Fig. 2.3a. Energy-weighted fluences from a source at 20 km incident on a detector in a geosynchronous orbit at different slant angles.

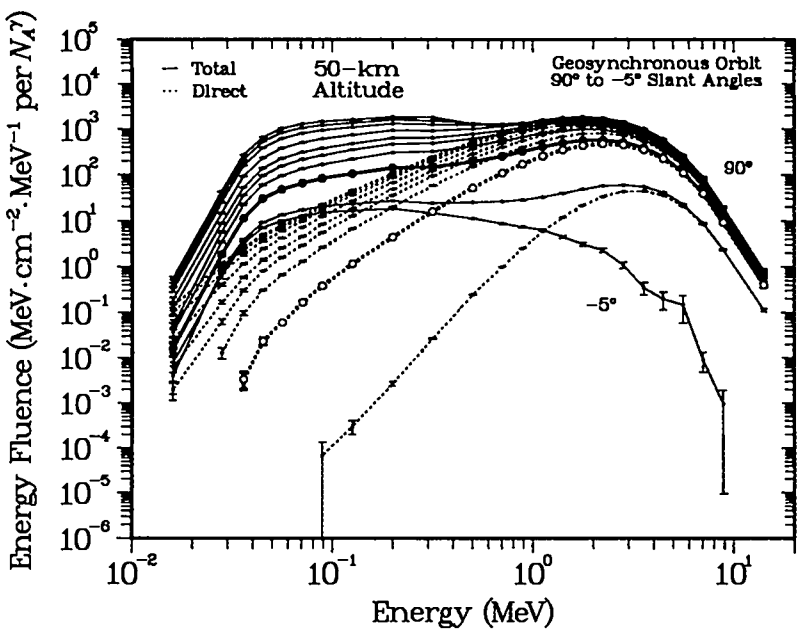

Fig. 2.3b. Energy-weighted fluences as in Fig. 2.3a, but for a source at 50 km.

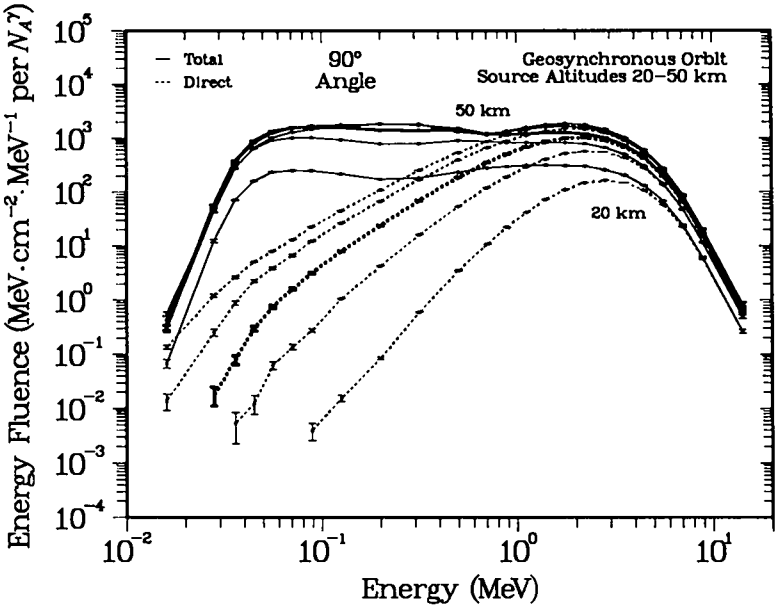

Fig. 2.4a. Energy-weighted fluences from sources with altitudes varying from 20 km to 50 km. The detector is in a geosynchronous orbit at a slant angle of 90°, that is, directly above the source.

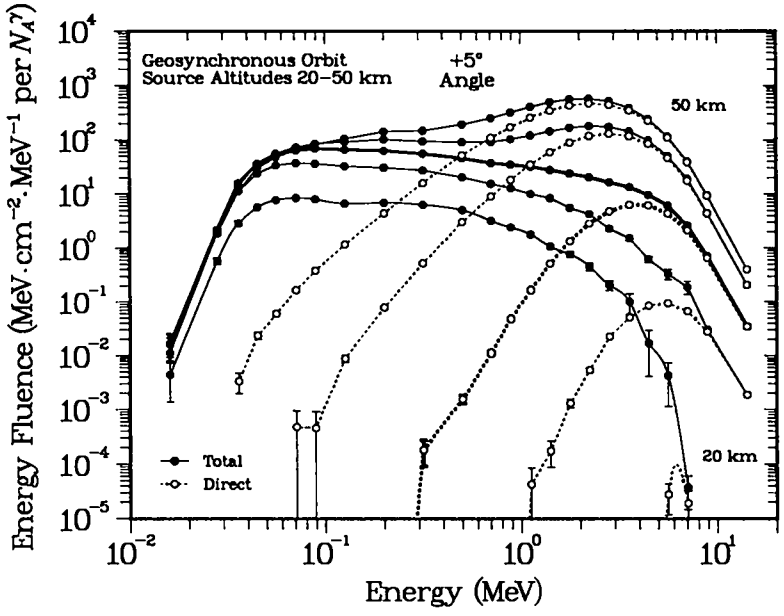

Fig. 2.4b. Energy-weighted fluences as in Fig. 2.4a, but for a slant angle of +5°.

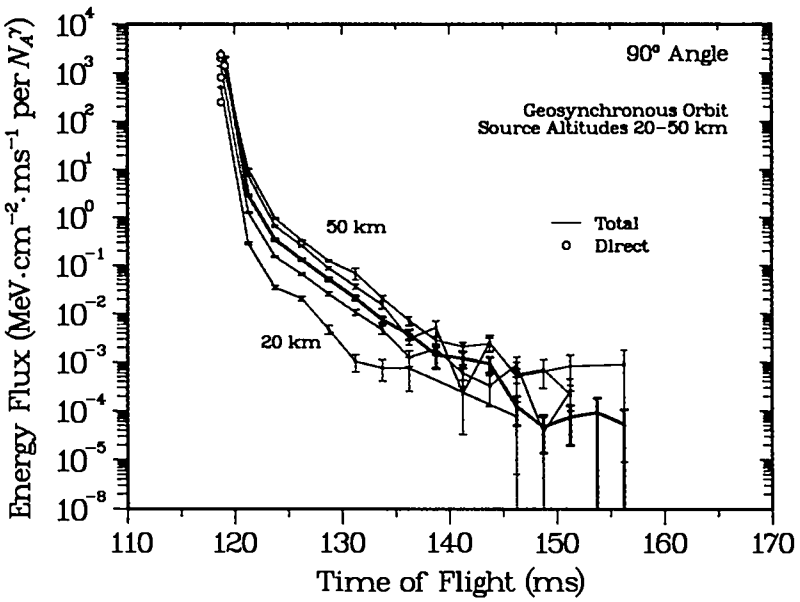

Fig. 2.4c. Differential time spectra of the photon energy flux from sources with altitudes varying from 20 km to 50 km. The geosynchronous detector is at a slant angle of 90°, that is, directly above the source.

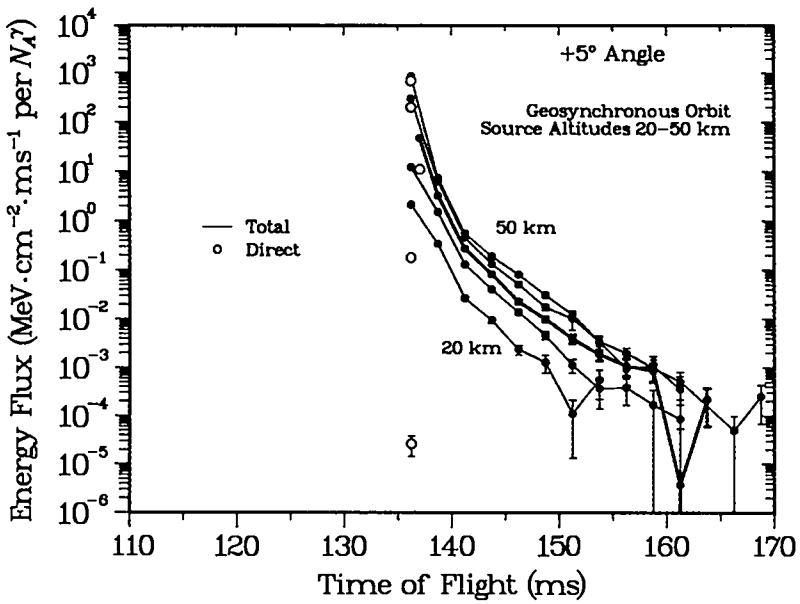

Fig. 2.4d. Differential time spectra as in Fig. 2.4c, but for a slant angle of +5°.

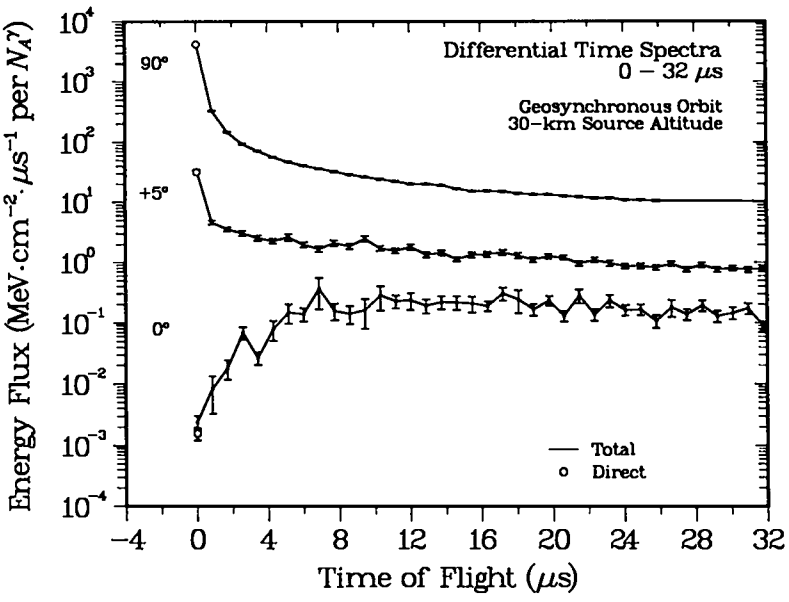

Fig. 2.5a. Differential time spectra for the photon energy flux at short times incident on a geosynchronous detector at slant angles of 0°, 5°, and 90° for a source at an altitude of 30 km.

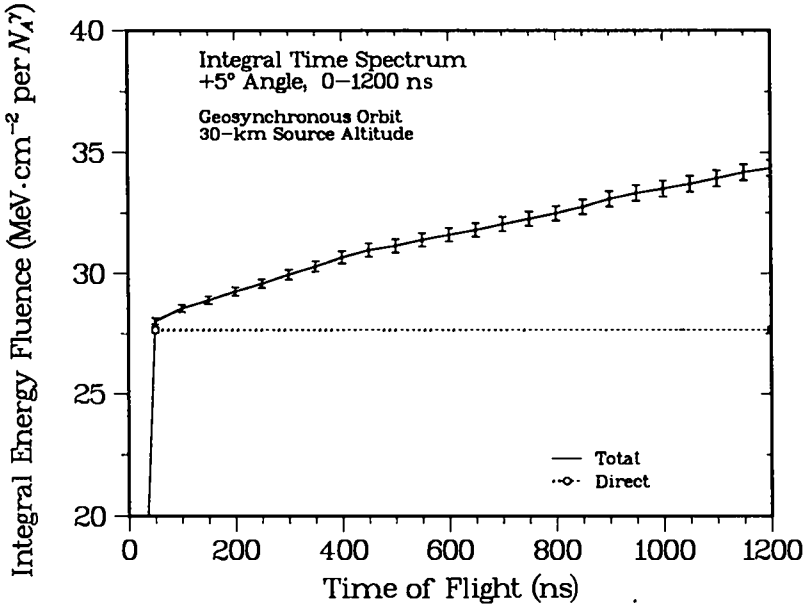

Fig. 2.5b. Time-integrated spectrum of the photon energy flux from 0–1200 ns incident on a geosynchronous detector at a slant angle of 5° above a source at an altitude of 30 km.

response of typical photon detectors, and it emphasizes that (1) the instantaneous step function at $t = 0$ combines with (2) a gradual increase at longer times to provide a signature that may be very distinct from the relatively abrupt impulse provided by detonations in free space or by typical environmental effects.

100-km Detector Orbits—Energy Spectra. We now shift our discussion of photon transport to a set of summary figures for a detector in a low orbit at 100 km. As stated in the geometry discussion for Fig. 1.1b, the atmospheric effects should be similar for both geosynchronous and lower orbits, because the atmospheric path lengths are almost the same. This point is emphasized by comparing the 100-km energy fluences in **Figs. 2.6a,b** with their geosynchronous counterparts in Figs. 2.4a,b. Other than the solid-angle difference of 5–6 orders of magnitude, the two sets of plots are almost interchangeable. We therefore suggest that many of our calculations for geosynchronous orbits can be used to estimate atmospheric effects for other orbits.

100-km Detector Orbits—Time Spectra. The similarities between the energy distributions for different orbits carry over to the corresponding time spectra, as shown in **Figs. 2.6c,d** (versus Figs. 2.4c,d). The initial intensities drop by 2–3 orders of magnitude in the first few tenths of milliseconds; this drop continues at a slower rate for a few tens of milliseconds, falling by another 8–10 orders of magnitude. This decay time is consistent with the time constant calculated by MCNP for low-energy capture, although the structure in the time-of-flight spectra suggests that competing effects are involved at different photon energies. The near-prompt part of the pulse presumably consists of photons that have undergone relatively few scatterings and remain at higher energies; the longer times are associated with many scatterings and lower energies. As with detectors in geosynchronous orbits, this "afterglow" behavior may provide a useful signature of an atmospheric detonation.

Direct versus Total Fluences. The discussions in this section have led to a interpretation in which photon energy fluences at the highest slant angles and source altitudes are scarcely different from their free-space counterparts, except that the time spectra always contain an afterglow that persists for several tens of milliseconds. As the path length increases at lower angles or altitudes, the time spectra lose their prompt peak, but the characteristic decay tail remains largely unchanged. Initially, the loss of photons to scattering has the result that the remaining fluence is generally direct in character—and hence more representative of the original source spectrum. Eventually, the scattering increases to the point that the high-energy photons themselves are shifted downward and then absorbed. This analysis leads to our final two figures in this section, **Figs. 2.7a,b**, which show the ratios between the direct and total fluences as functions of slant angle and source altitude. Above our selected cutoffs at 30 km and +5°, the direct fluences are seen to be almost always greater than 50% of the total values. For detectors with some discrimination against photons at lower energies, it is likely than even higher direct-to-total fractions can be obtained. In any case, at lower source altitudes or slant angles these ratios change rapidly and may provide useful information about the source location.

Summary. The integral results at the beginning of this section establish that both photon transmissions and the energy fluences are near their free-space limits at the highest source altitudes or slant angles, but they fall off rapidly below about 30 km or 5° above the horizon. The falloff in the direct, unscattered portion of the fluence is more abrupt than that for the total fluence, which leads to a set of differential analyses in terms of energy and time dependence. The differential-energy results show that the high-energy fluence is mostly uncollided photons and that scattered photons dominate the fluences at lower energies. Hence, for higher source altitudes and slant angles it appears that the rate of photon downscattering in energy is greater than the rate of loss to low-energy absorption.

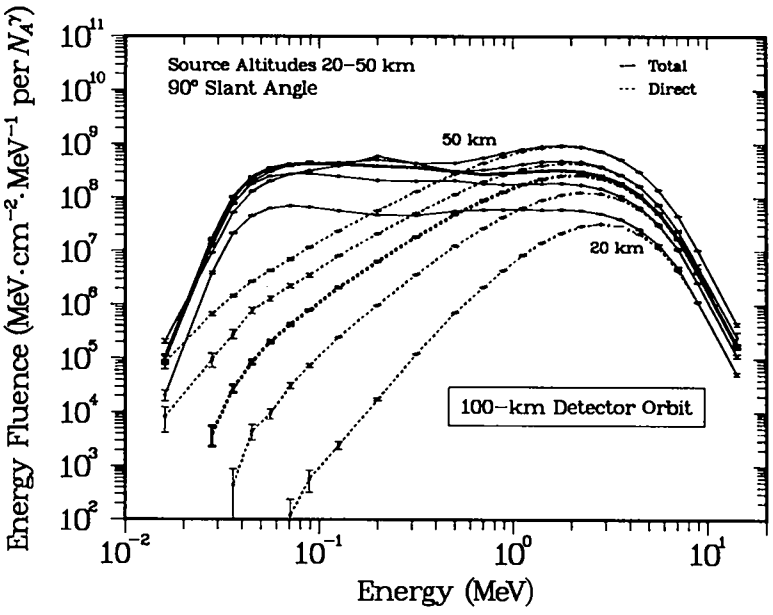

Fig. 2.6a. Energy-weighted photon fluences from sources with altitudes varying from 20 km to 50 km. The detector is in a 100-km orbit and is directly above the source.

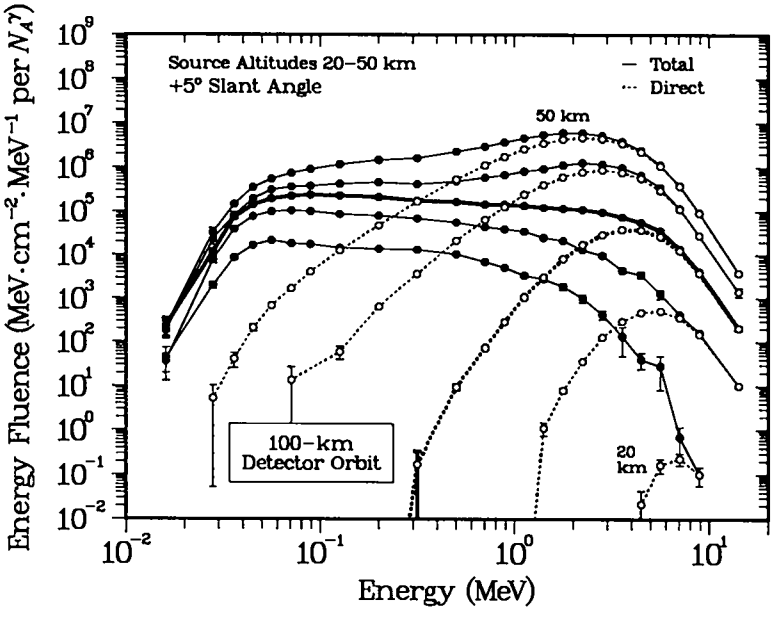

Fig. 2.6b. Energy-weighted fluences as in Fig. 2.6a, but for a slant angle of $+5^{\circ}$.

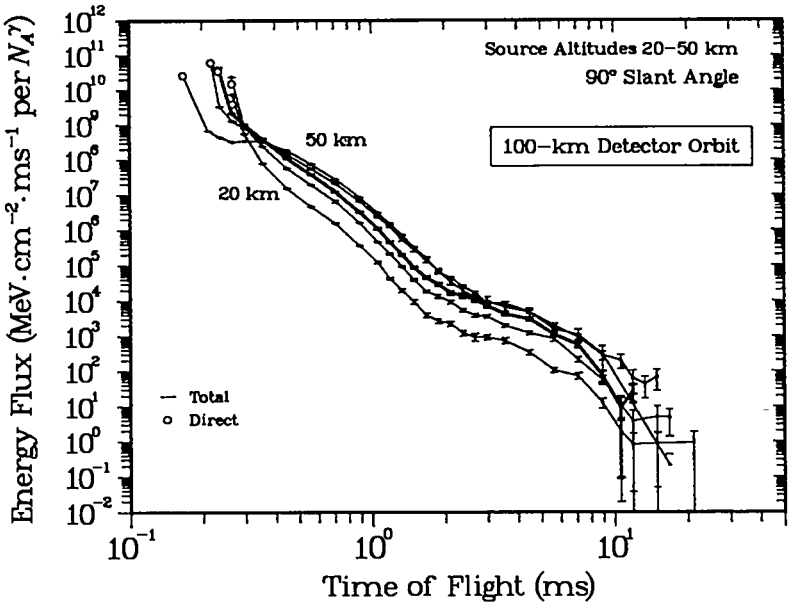

Fig. 2.6c. Differential time spectra of the photon energy flux from sources with altitudes varying from 20 km to 50 km. The detector is located in a 100-km orbit and is directly above the source.

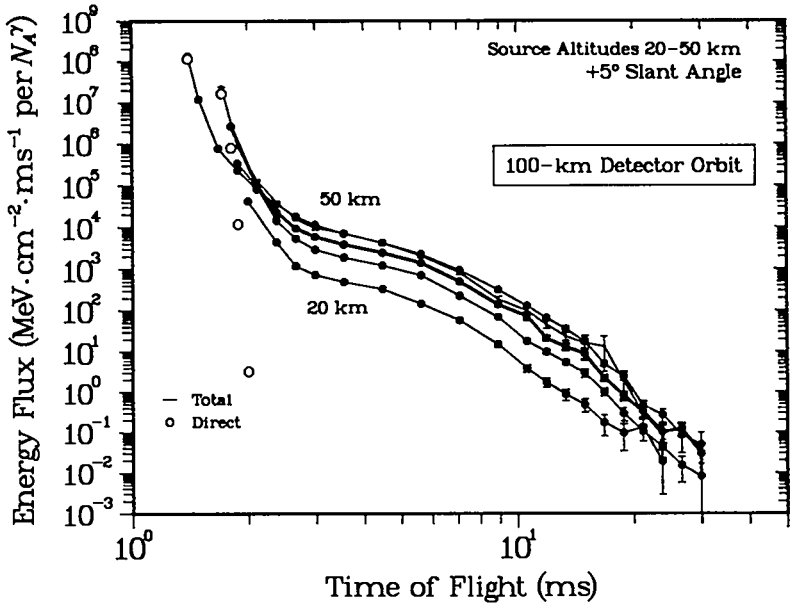

Fig. 2.6d. Differential time spectra as in Fig. 2.6c, but for a slant angle of $+5^{\circ}$.

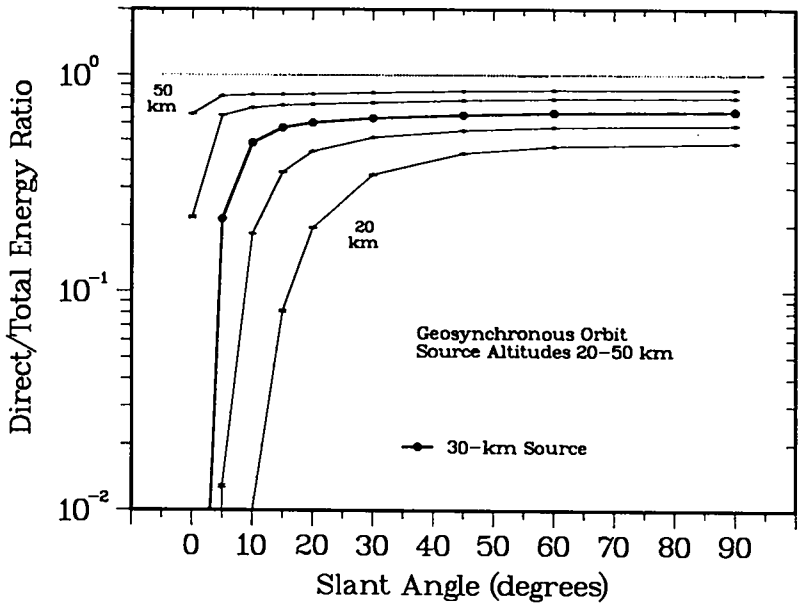

Fig. 2.7a. Unscattered fraction of the total photon energy as a function of slant angle.

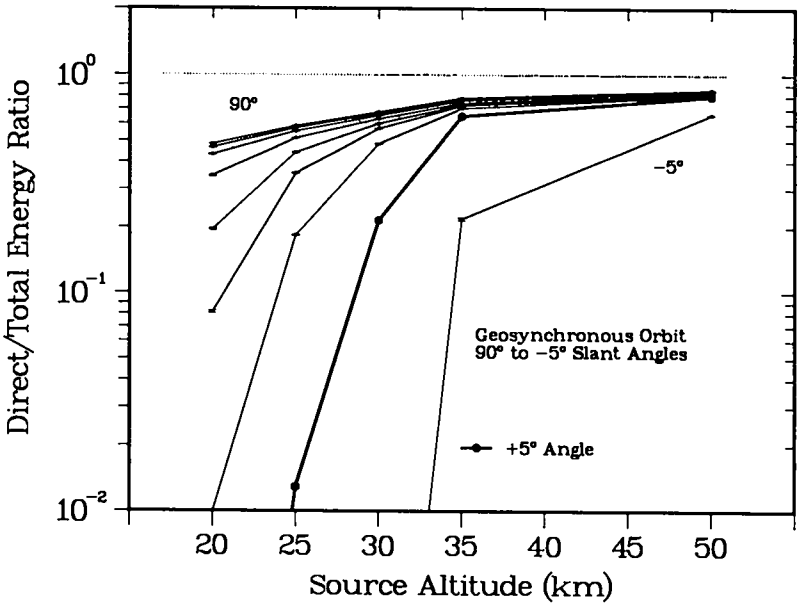

Fig. 2.7b. Unscattered fraction of the total photon energy versus source altitude.

The differential-time results, particularly for the earliest times, show that the unscattered high-energy flux arrives at the detector in a sharp burst, and the scattered lower-energy photons gradually arrive over the next 20–40 ms. This afterglow behavior is a characteristic of atmospheric scattering; it does not exist in free space, nor is it typical of environmental backgrounds. Because the path lengths in the atmosphere are essentially the same for both geosynchronous and lower orbits, the energy and time results for both cases are the same except for $1/r^2$ scaling factors. Finally, the results in this section can be summarized in terms of the direct-to-total ratios of the fluences arriving at the detector. Because only the direct fluence contains useful information about the source, these ratios are a straightforward measure of the effect of atmospheric scattering. Thus, the most important results are (1) the source-altitude and slant-angle cutoffs, (2) the connection between the direct fluence and high photon energies, (3) the characteristic scattered-photon afterglow in the time spectra, and (4) the interpretation in terms of direct-to-total fluence ratios.

3. NEUTRON CALCULATIONS

Overview. The presentation of our neutron-transport calculations is similar to that used in the previous gamma-ray section. As before, we begin with summaries of the slant-angle and source-altitude dependence of the fluences integrated over both energy and time. Because neutron detectors do not respond directly to neutron energy, the results are plotted only as particle transmissions, not energy fluences. However, separate calculations are shown for both fusion and fission sources as functions of slant angle and source altitude. We then briefly examine the correlation between the actual neutron energy at the detector and apparent energy as determined from the neutron time of flight. As in free space, this correlation makes it possible to interpret time-of-flight measurements in terms of neutron energies. The resulting differential information is presented as both energy and time spectra, first for simple fusion sources, then for fission-only sources, and finally for mixed fission/fusion sources. In each case the discussion includes angle and altitude variations as well as direct versus total fluences. After presenting similar results for 100-km orbits, we close with a summary that compares the neutron and gamma-ray results.

Integral Transmissions—Angle Dependence. As in the photon discussion, neutron transmissions are defined relative to the fluence that would be observed for transport in free space. **Figures 3.1a,b** show the results for fusion and fission sources as functions of slant angle. The direct fluences in both cases are very similar, indicating that the interaction mechanisms for MeV-range neutrons change only slowly. Surprisingly, however, the total fluxes are also very similar, despite the considerable difference between the reaction channels available for high- and low-energy neutrons. Our conclusion is that the transport mechanisms are probably dominated by scattering effects, not absorption. Accordingly, for both fission and fusion sources, the total fluence exceeds the free-space limit over a wide range of source altitudes and slant angles. Although the direct transmissions are generally quite low, the total transmissions are comparable with our previous results for photon transport. As in those analyses, the fluences drop rapidly below about $+5°$, and we have emphasized the 30-km results by using plotting symbols and heavier lines.

Integral Transmissions—Altitude Dependence. The similarity between the fission and fusion results, as well as the difference between the direct and total neutron fluences, is also apparent in the altitude-dependent results shown in **Figs. 3.2a,b**. This direct-versus-total difference becomes increasingly obvious in comparisons beyond the reference cases of $+5°$ and 30 km. Thus, although the rates of falloff for the fluence versus slant angle and source altitude are very similar to the photon cases, for neutrons there

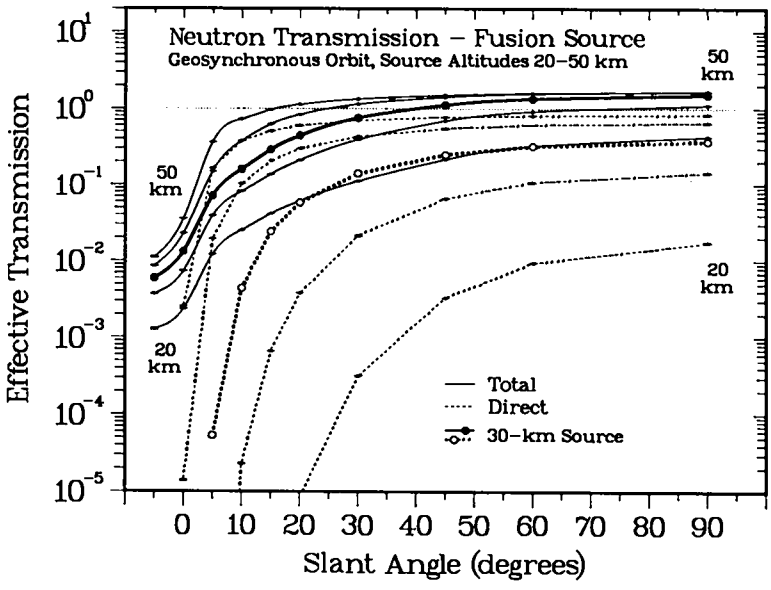

Fig. 3.1a. Angular dependence of the direct and total neutron fluences for fusion sources at different altitudes, after integration over both energy and time.

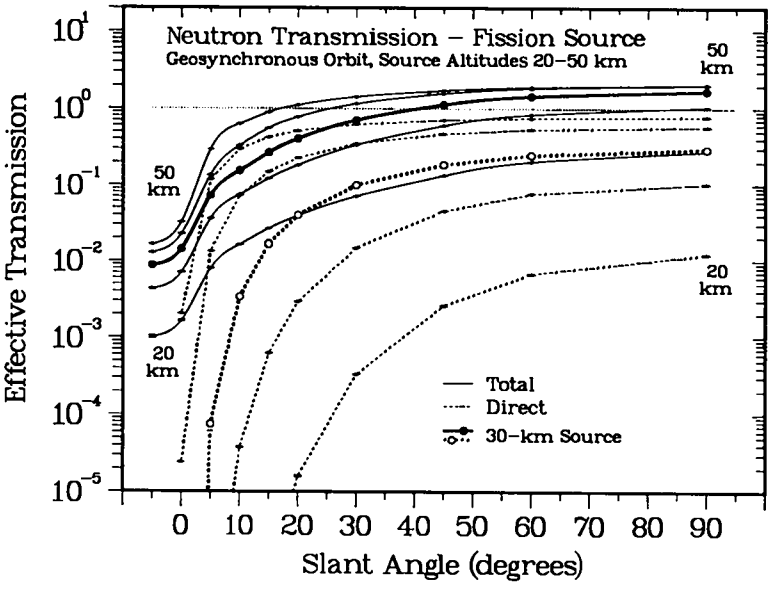

Fig. 3.1b. Angular dependence of the direct and total neutron fluences for fission sources at different altitudes, after integration over both energy and time.

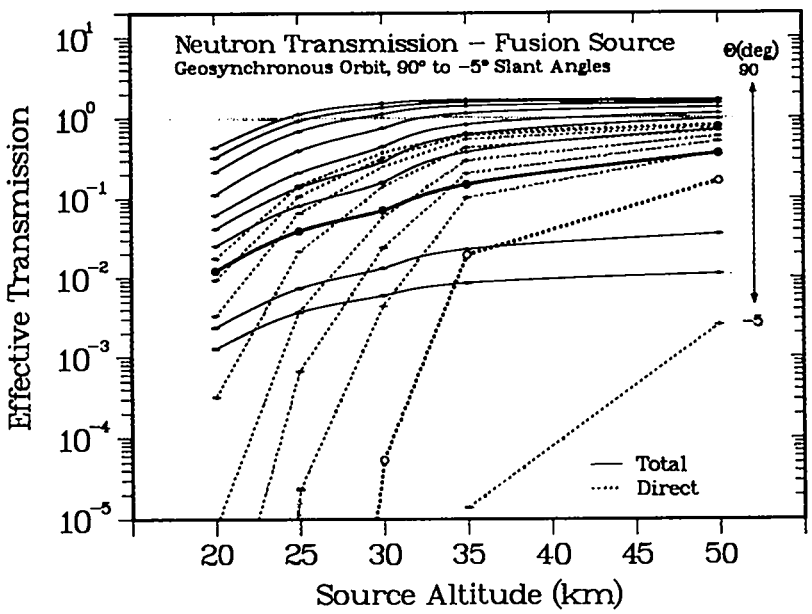

Fig. 3.2a. As in Fig. 3.1a, but for the altitude dependence of the integrated fusion fluences at different slant angles.

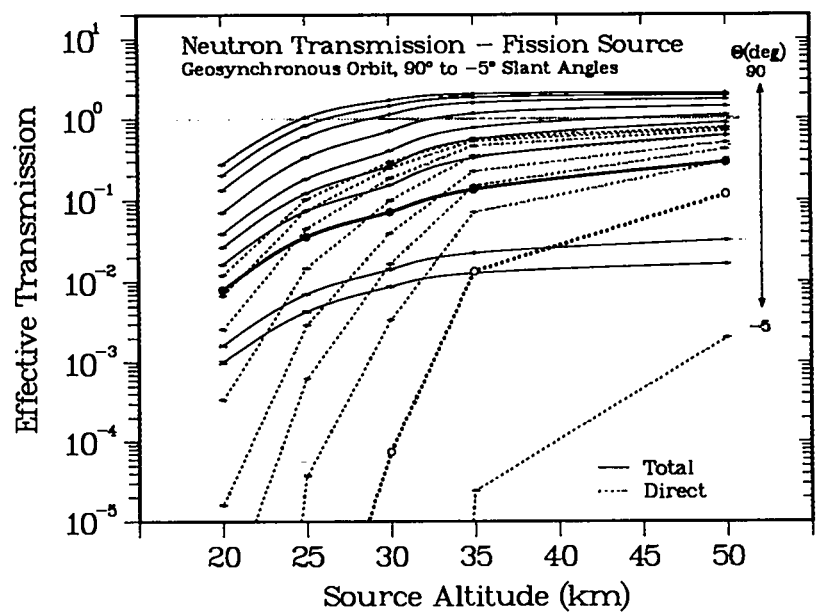

Fig. 3.2b. Transmissions as in Fig. 3.1b, but for altitude dependence.

are much larger differences between the magnitudes of the direct versus total transmission values.

Direct-to-Total Ratios—Angle and Altitude Dependence. The comments on the direct and total fluences for neutrons are emphasized by the two plots of direct-to-total ratios presented in **Figs. 3.3a,b.** In Fig. 3.3a, the rapid falloff below slant angles of 5–10° is clear; Fig. 3.3b shows a slightly more gradual version of the same behavior near source altitudes of 30–35 km. These figures reveal two additional points. The first is the near-identity of fission and fusion ratios, which is made obvious by the overlays in the two figures. This agreement is a result of the surprising similarity between the fission and fusion transmissions themselves, which was seen in the previous pairs of figures. As a result, we can ignore most of the energy dependence of the neutron transport mechanism in our discussion. The second point involves the neutron and gamma-ray transport mechanisms. For gamma rays, the direct-to-total ratios in Figs. 2.7a,b exceed 50% at many source altitudes and slant angles; the neutron ratios in Figs. 3.3a,b reach this level only in the few most favorable cases. This behavior suggests that, when compared with the rapid energy loss and particle absorption seen for gamma-ray transport, neutron scattering causes relatively less energy loss and much less absorption.

Comparison with Previous Integral Results. We conclude our discussion of integral fluences with a comparison between the present calculations and the previous results in Ref. 5, which included only a 90° slant angle but extended to much lower source altitudes. **Figure 3.4** repeats the current total fluences for 90°, averaged over the fission and fusion results, and adds the lower-altitude values from Ref. 5. The two sets of calculations agree well at 20 km; the dramatic transmission rolloff at lower source altitudes can be appreciated by noting its power-law behavior, which follows roughly the 16th power of the decreasing altitude.

Time-of-Flight versus Energy Correlations. For a more detailed transport analysis, we now turn to the differential energy and time behavior of the fluences. As preparation, in **Fig. 3.5** we show the relationship between the actual neutron energy as observed at the detector location and the apparent neutron energy as computed from the neutron time of flight. Each point corresponds to the mean energy for one of the MCNP time tallies, with one set for each of the two source distributions. There is a slight systematic difference between the two sets, especially at high energies. For transport in free space, the actual and detected energies would agree trivially and follow the diagonal line in the figure. For atmospheric transport, however, maintaining this relationship requires the unlikely result that the energy loss in scattering exactly balance the additional flight time along the indirect path to the detector. In our case, the time increase is slightly larger than the energy loss, but the two quantities remain correlated (as seen in previous transport studies[7]). Such a correlation is essential for obtaining useful information about the neutrons from atmospheric sources. In fact, a useful MCNP option exists to tally the time of flight versus the original source energy, thereby directly providing the necessary conversion function.

Fusion Source at a 30-km Altitude. Although neutron energies are not directly observable at the detector, their calculation is more straightforward than that for the time-of-flight presentation. **Figures 3.6a,b** show the simplest case, a nearly monoenergetic fusion source at a 30-km altitude. As indicated by the dashed curves, the loss of direct fluence increases at lower slant angles, with the result that at +5° the original peak has almost disappeared and the direct fluence has dropped by about 4 orders of magnitude from the 90° value. In the total spectra (solid curves) at all slant angles, neutrons scattered from the atmosphere around the source create a pronounced shoulder on the fusion peak and an undulating tail extending downward to well below 1 MeV. The prevalence of the

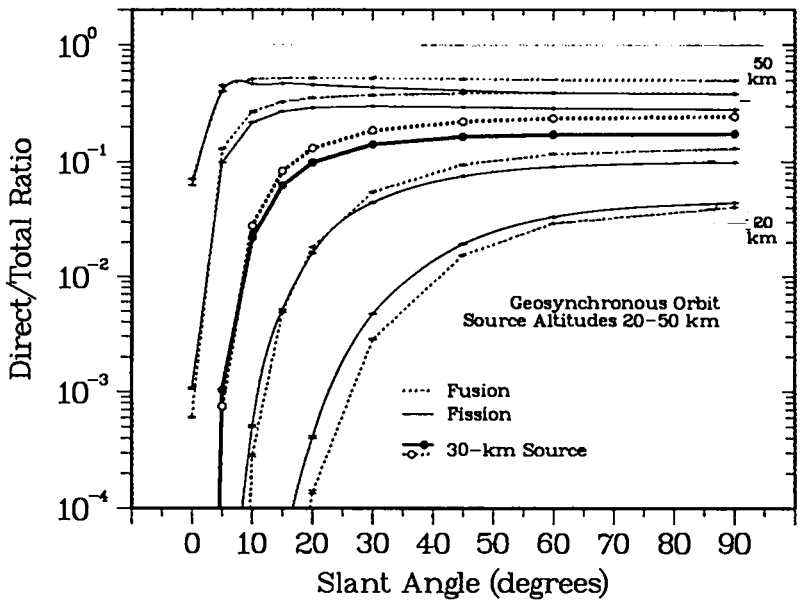

Fig. 3.3a. Direct-to-total ratios for fission and fusion sources as a function of slant angle.

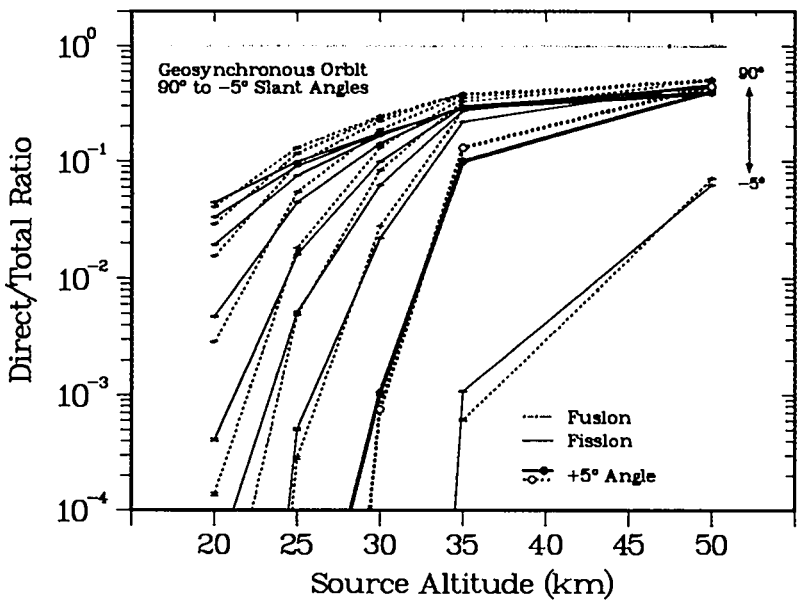

Fig. 3.3b. Direct-to-total ratios for fission and fusion sources as a function of source altitude.

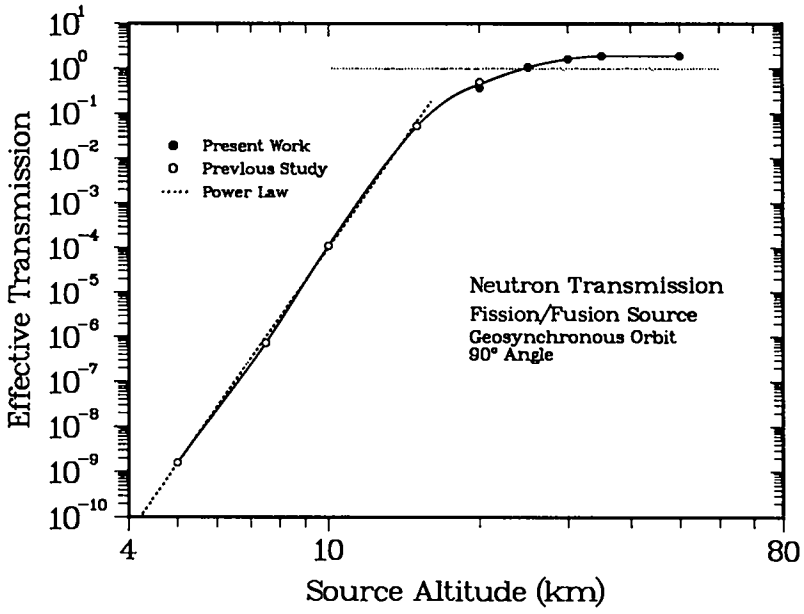

Fig. 3.4. Total flux transmissions as a function of source altitude for a fission/fusion source viewed at 90°, including previous calculations.

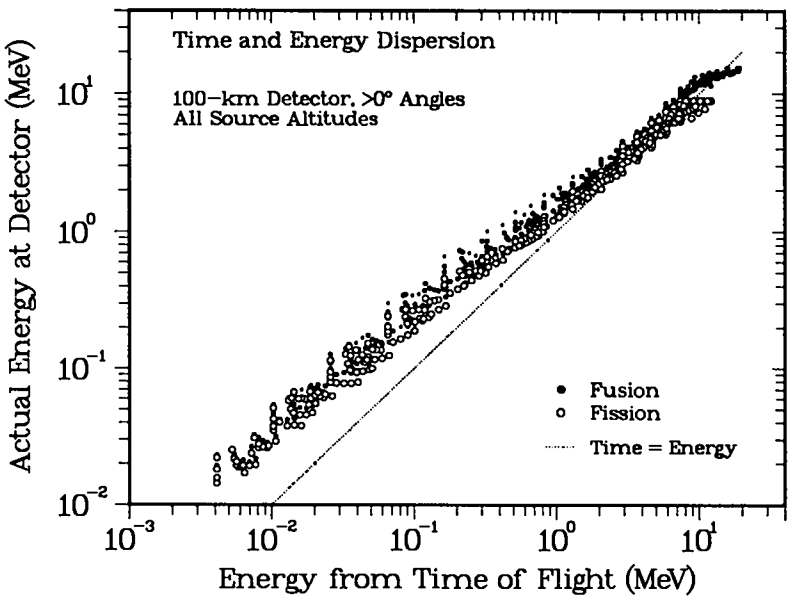

Fig. 3.5. Locus comparing neutron energies as determined by time of flight with the actual energies at the detector. The line shows the trivial free-space relationship.

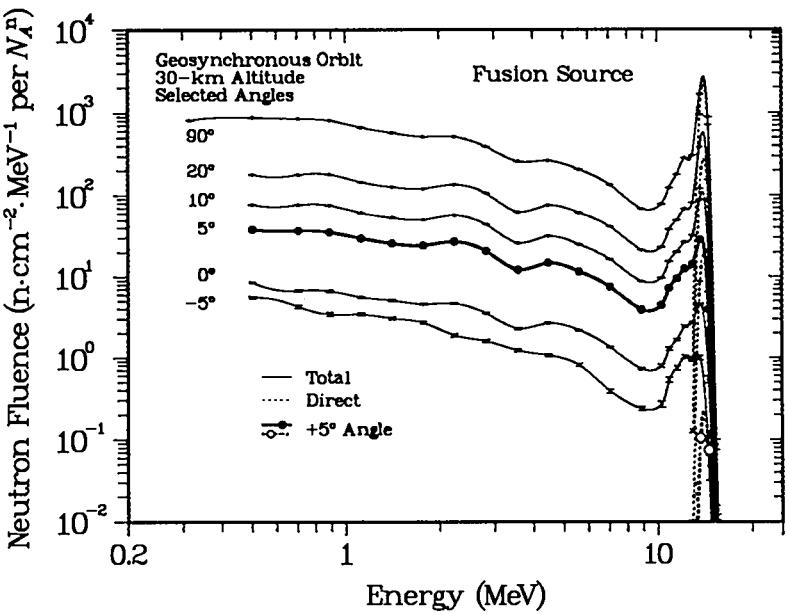

Fig. 3.6a. Angular variation of the neutron energy spectrum from a fusion source at 30 km as observed at a geosynchronous detector, showing both direct and total fluences.

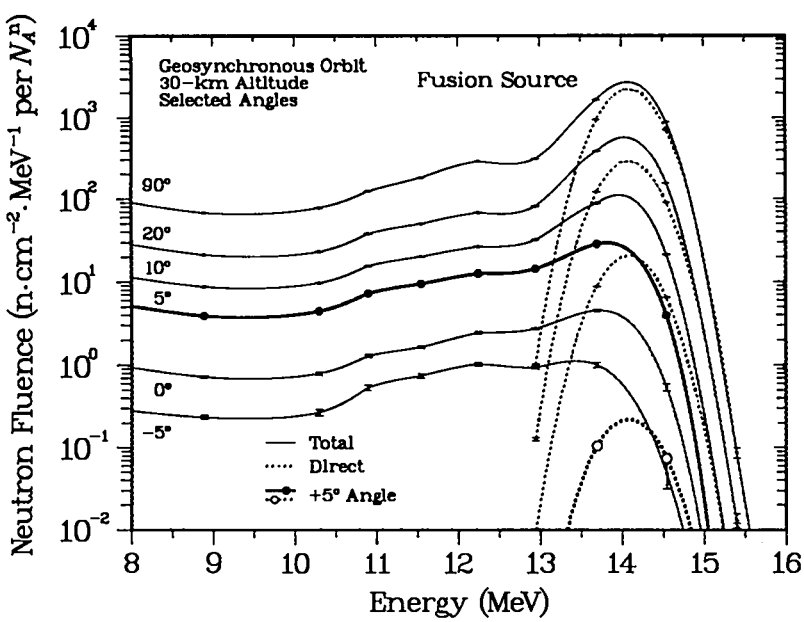

Fig. 3.6b. Detail of the high-energy portion of Fig. 3.6a, emphasizing the long tail and the changing contribution from the direct component.

structure at all slant angles suggests its origin is air-transport effects. The distortion is seen more clearly in the expanded view of Fig. 3.6b. Even along the leading edge of the fusion peak, the direct fluence dominates only near 90°; all peaks at lower slant angles are distorted by scattering. For reference, the free-space spectrum would be similar to the direct 90° case shown here, but with a magnitude about 3 times greater (based on the transmissions in Fig. 3.1a).

Fusion Source—Time Dependence. Although the interpretation of the energy spectra in Figs. 3.6a,b is straightforward, the only measurable neutron observable is the time of flight, not the energy. Accordingly, **Fig. 3.7a** shows the time-of-flight equivalent of the energy spectrum in Fig. 3.6a. Although the two spectra are qualitatively similar, differences in resolution make it difficult to precisely associate the different structures. Fortunately, the apparent lack of time resolution is a calculational problem, not an actual time smearing. Although narrow steps across an energy peak can be specified easily, obtaining the corresponding fine time resolution requires defining a separate set of time bins at each source altitude and slant angle to account for the changing flight path. To illustrate, **Fig. 3.7b** shows a single high-resolution time-of-flight calculation for the +5° case shown in Fig. 3.7a. By comparing the high-resolution energy and time spectra in Figs. 3.6b and 3.7b, we note a one-to-one correspondence between the two sets of structures. We also see that the standard resolution may be adequate at lower energies, but it cannot be relied on for precise information near the high-energy fusion peak.

Fission Source at a 30-km Altitude. Because the fission source has an energy dependence that is more complex than the fusion source, simple trends are difficult to identify and only a few figures will be shown here. **Figure 3.8a** shows energy spectra from a source at 30 km for two extreme slant angles, 90° and +5°. At the lower angle, the direct fluence dramatically shows the structure associated with transmission through the nitrogen and oxygen in the atmosphere. As discussed in Ref. 8, the overlapping of resonances in these two nuclei leads to broad transmission maxima near 1.0, 2.5, and 5 MeV, just as seen here and in the preceding fusion results. This structure, however, is of little practical significance, because the direct component makes up only a small fraction of the total observed fluence. Only at the highest slant angle, and then only at the highest energies, does it provide a dominant contribution. At the lower slant angles, the direct component is always orders of magnitude lower than the scattered one. This behavior is seen also in the corresponding time-dependent plot shown in **Fig. 3.8b**. Although the correlation between energy and time of flight carries the energy structure over into the time spectrum, only a hint of the resonances exists in the total fluence. These resonances, however, may be useful for establishing the source range. Of course, no such structure would be seen in the free-space flux; according to the transmissions in Fig. 3.1b, its magnitude would be about twice that of the total spectrum shown in Figs. 3.8a,b. Here it is important to remember that energy-dependent scattering affects the shapes of both the direct and total fluxes, so that neither result matches the shape of the original free-space source spectrum.

Fission/Fusion Source at a 30-km Altitude. Having examined the fusion and fission cases separately, we now turn in the next several figures to a 1:1 mixed fission/fusion source, which we obtain by simply combining the results from the two separate cases. Because the integral values for the fusion and fission cases are almost identical (see Figs. 3.1a,b), the values for the mixed case need not be shown here. The differential analysis opens with **Fig. 3.9a**, which shows energy spectra at the two angular extremes of 90° and +5°. It is no surprise that only fusion neutrons contribute at high energies and early times, but the breakdown into the separate components shows that the downscattered fusion tail remains significant all the way to the peak of the fission distribution. This behavior exists at both slant angles, and it appears also in the corresponding time-of-flight

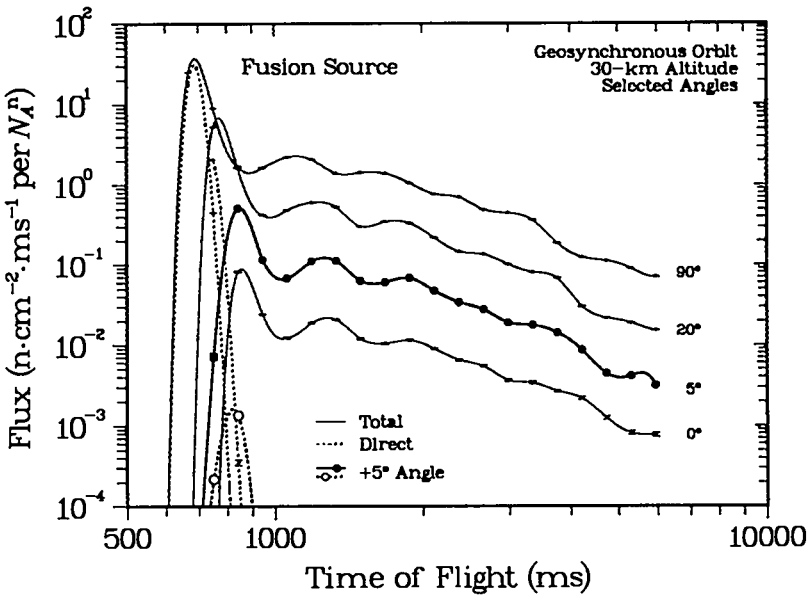

Fig. 3.7a. Angular variation of the neutron time-of-flight spectrum from a fusion source at 30 km as observed at a geosynchronous detector, showing both direct and total fluences.

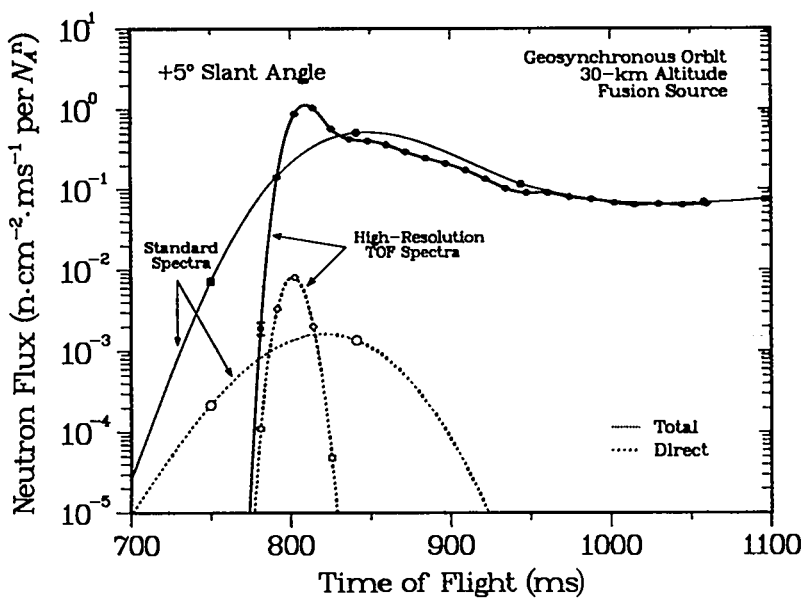

Fig. 3.7b. Detailed calculation of the time-of-flight spectrum for a 30-km source altitude and +5° slant angle, emphasizing the importance of fine time steps at high energies.

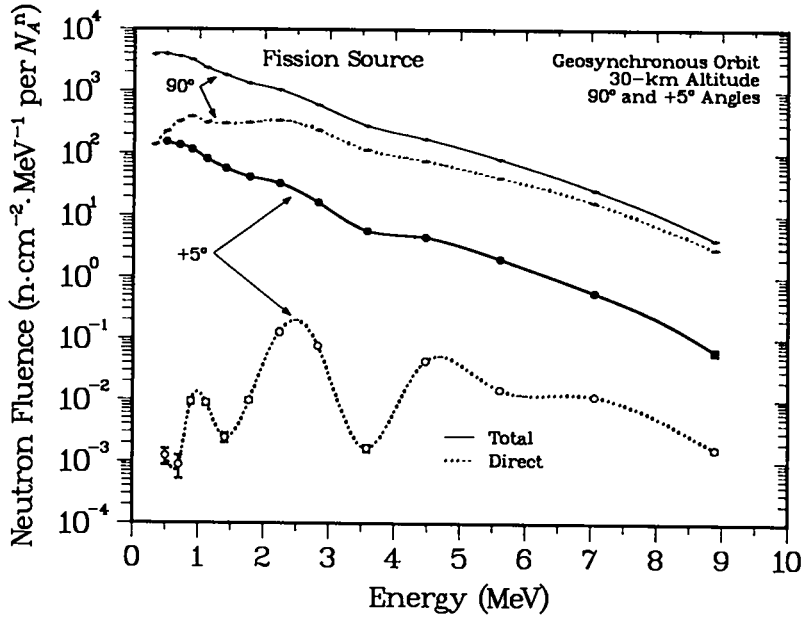

Fig. 3.8a. Neutron energy spectra from a fission source at 30 km as observed at a geosynchronous detector, showing both direct and total fluences at two slant angles.

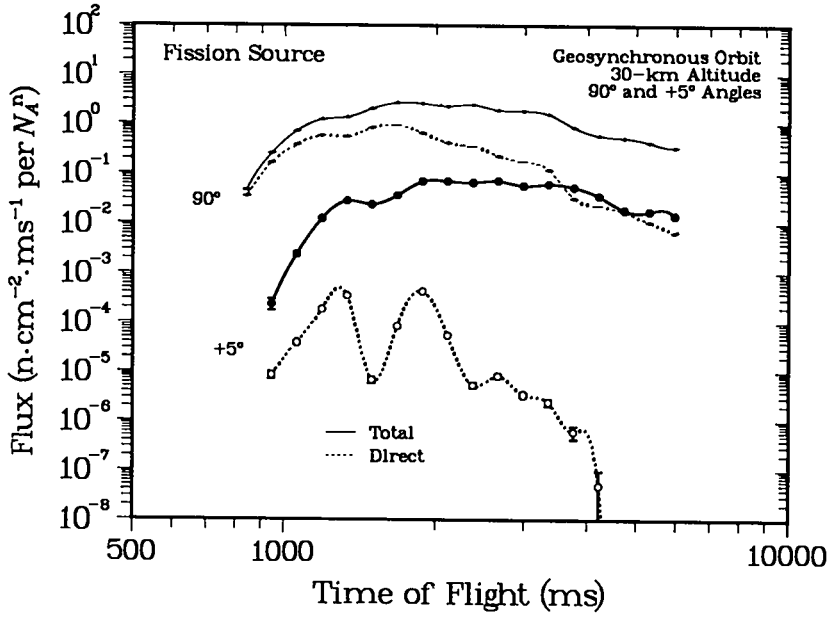

Fig. 3.8b. Fission spectra as in Fig. 3.8a, but presented as time-of-flight data.

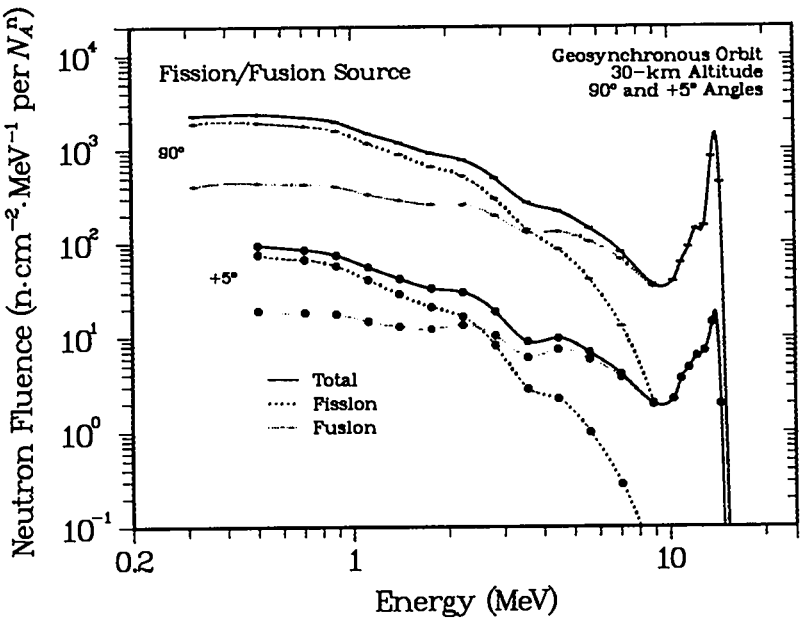

Fig. 3.9a. Neutron energy spectra from a fission/fusion source at 30 km as observed at a geosynchronous detector for two different slant angles.

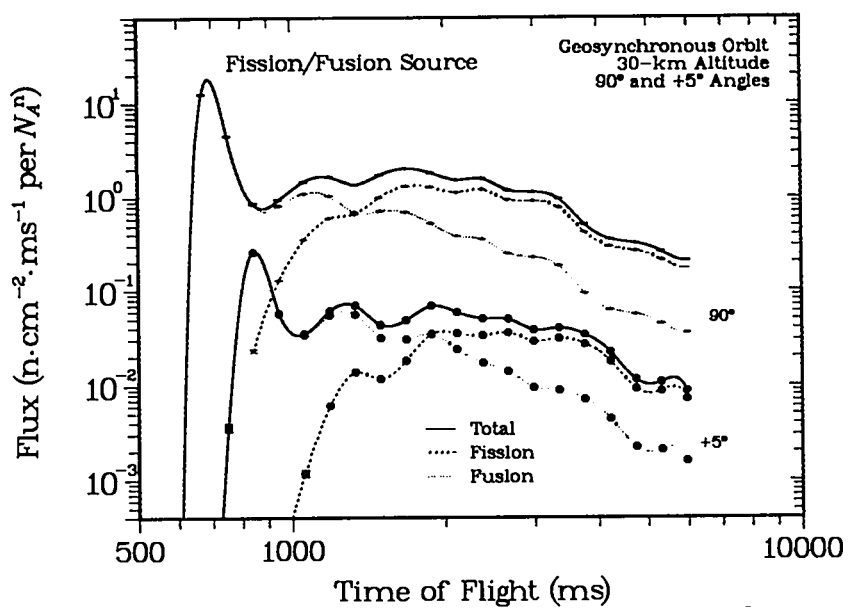

Fig. 3.9b. Fission/fusion spectra as in Fig. 3.9a, but presented as time-of-flight data.

spectra shown in **Fig. 3.9b**. Again, the lack of detail in the fusion peak is caused by the limited resolution of the calculation, not by actual time smearing.

Fission/Fusion Source—Extreme Altitudes and Angles. In **Figs. 3.10a,b** we examine the time-of-flight spectra at the extreme useful limits of our calculations, that is, at source altitudes of 20 and 50 km and slant angles of 90° and +5°. The most interesting result is the generally greater downscattering of the fusion peak at low source altitudes compared with low slant angles. This effect is also seen in the direct-to-total ratios in Figs. 3.3a,b. At 50 km (Fig. 3.10a), the fusion peak stands out clearly, and the downscattered flux interferes only slightly with the lower-energy fission component. At 20 km (Fig. 3.10b), the fusion component is a major contribution at all time-of-flight values. This behavior, with source altitude having a greater effect than slant angle, contrasts with the observations for the gamma-ray case and with the results from the integral discussion. A second feature of these figures is the pronounced resonance structure in the total spectra, which at low source altitudes exists even in the fusion case. To provide some idea of the overall variation, in **Figs. 3.11a,b** we show sets of total spectra at our two extreme slant angles for all source altitudes. For the 90° case (Fig. 3.11a), the spectra at the highest source altitudes change very slowly. For the +5° case (Fig. 3.11b), however, each decrease in altitude causes pronounced changes in both magnitude and shape. In the worst cases, the fusion peak almost completely disappears. This behavior again suggests that scattering, not absorption, is the dominant issue in neutron transport, a result different from the model for our photon analyses.

Fission/Fusion Source for a 100-km Orbit. For a given source altitude and slant angle, the path length in the atmosphere is the same for all detector orbits. Qualitatively, therefore, the fission/fusion relationships for a 100-km orbit should be similar to those for the geosynchronous orbit. This hypothesis is verified by **Figs. 3.12a,b**, which show the energy and time-of-flight spectra for a 30-km source viewed at the two extreme slant angles (for comparison with Figs. 3.9a,b). Again, the scattering effects are well resolved in the energy spectrum, but the limited bin sizes make their identification more difficult in the calculated time spectra.

Fission/Fusion versus Fission-Only Sources. The downscattering of the fusion peak for low source altitudes and slant angles raises questions about the distinguishability of the two important cases of fission-only versus combined fission/fusion sources. **Figures 3.13a,b** show the angle dependence of the 30-km versions for these two sources. The two cases are easily separated, even for the most distorted examples. However, the mixed fission/fusion spectra presented above make it clear that simply distinguishing between the fission-only and fission/fusion sources cannot provide accurate information about important parameters such as fission-to-fusion ratios. Downscattered fusion neutrons contaminate the spectrum even at lower energies, and relating the observed total spectrum to the one observed in free space is complicated at every source altitude studied.

Direct and Total Spectra—Moderate Cases. Because so many of our analyses have focused on the extreme ends of the angle and altitude ranges, we include here two figures that illustrate the behavior of more intermediate cases. **Figures 3.14a,b** show examples that represent combinations at the most favorable slant angle (90°, at 35 km) and source altitude (50 km, at 15°). For the 90° case, even at the relatively high source altitude of 35 km the direct flux is dominant only along the leading edge of the fusion peak. For all subsequent times, the scattered flux provides the majority of the response. Similar behavior is seen for the 50-km, 15° spectrum. This similarity should be expected based on Fig. 3.3b, which shows that these cases are among a large number of combinations with nearly the same direct-to-total ratios. More important, however, is the comparison with the free-space fluences indicated in Fig. 3.1a,b. Although the direct-to-total ratios for

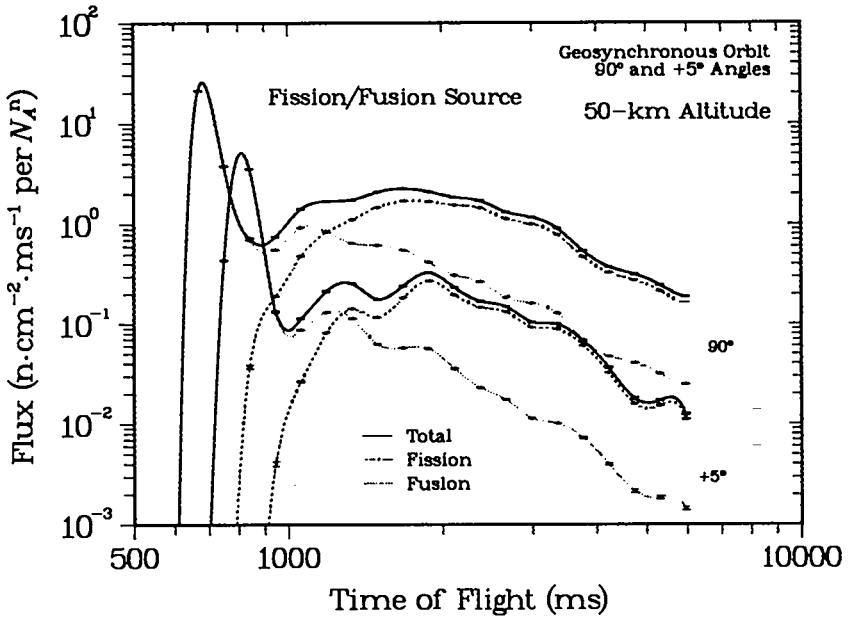

Fig. 3.10a. Neutron time-of-flight spectra from a fission/fusion source at 50 km as observed at two extreme slant angles.

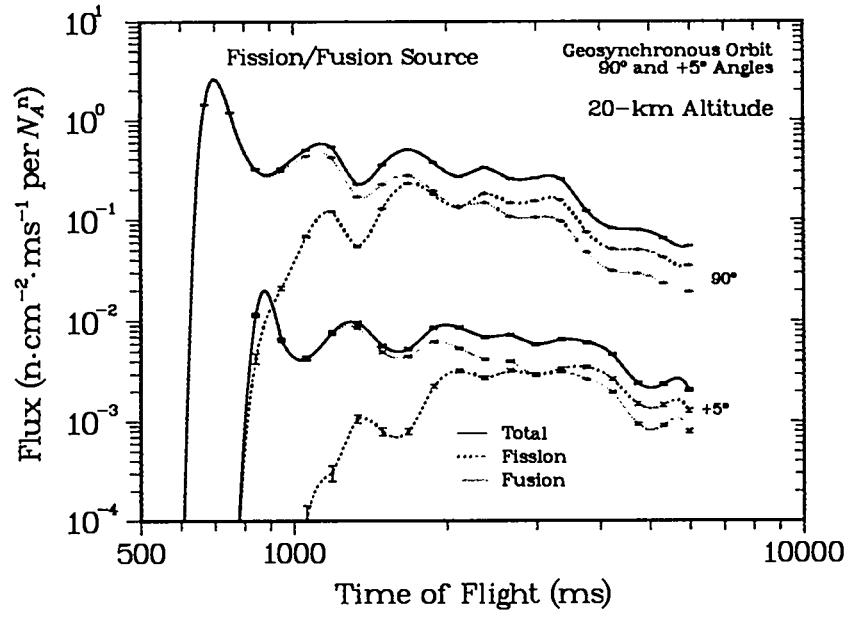

Fig. 3.10b. Neutron time-of-flight spectra as in Fig. 3.10a, but for a 20-km source altitude.

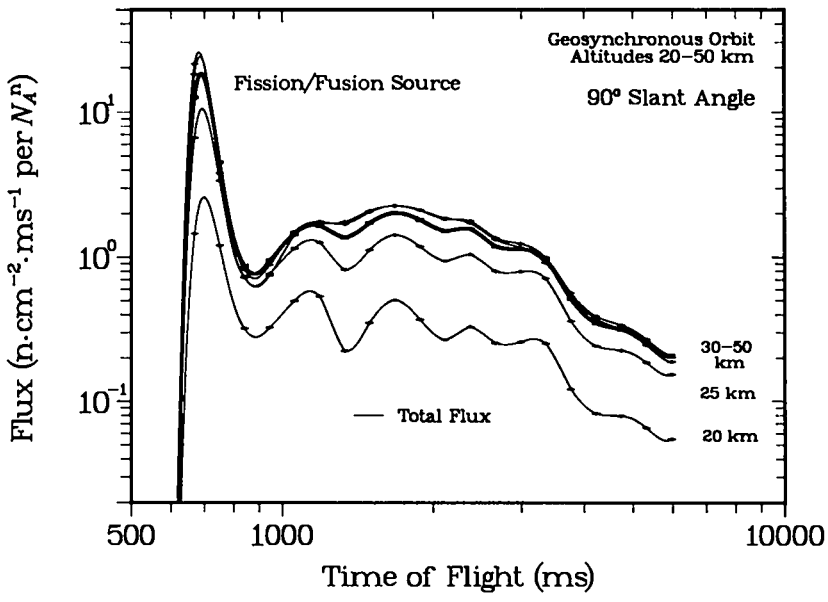

Fig. 3.11a. Neutron time-of-flight spectra from fission/fusion sources at 20–50 km as observed in a geosynchronous orbit using an extreme slant angle of 90°.

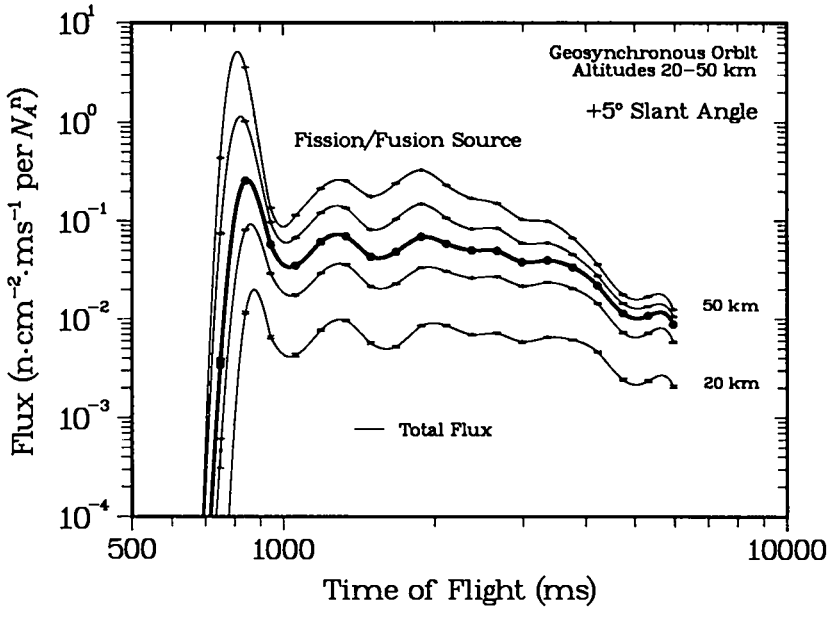

Fig. 3.11b. Neutron time-of-flight spectra as in Fig. 3.11a, but for a slant angle of +5°.

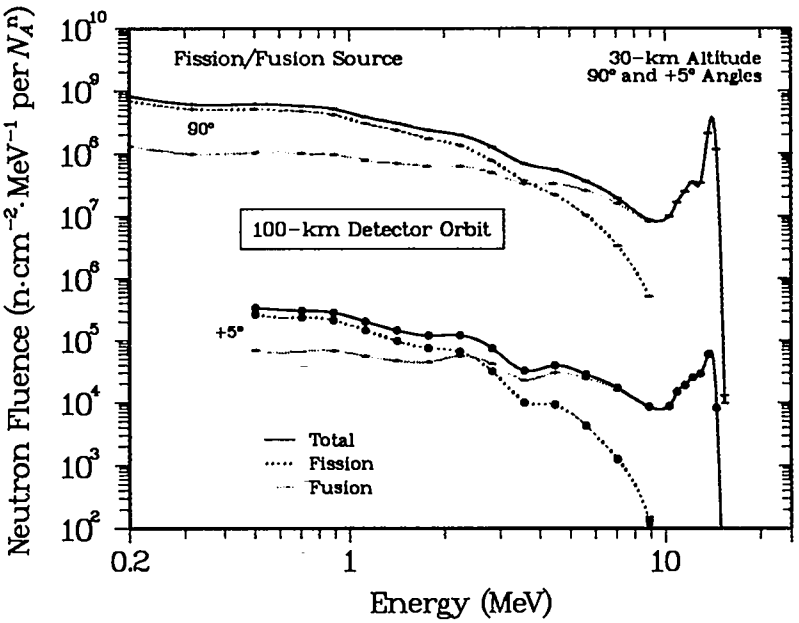

Fig. 3.12a. Neutron energy spectra from a fission/fusion source at 30 km as observed in a 100-km orbit for two different slant angles.

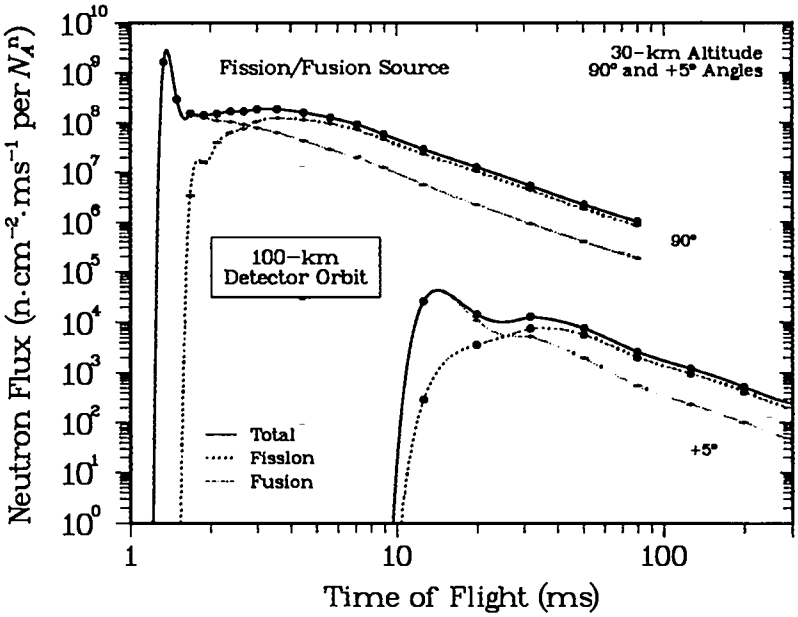

Fig. 3.12b. Neutron time-of-flight spectra corresponding to the energy spectra of Fig. 3.12a.

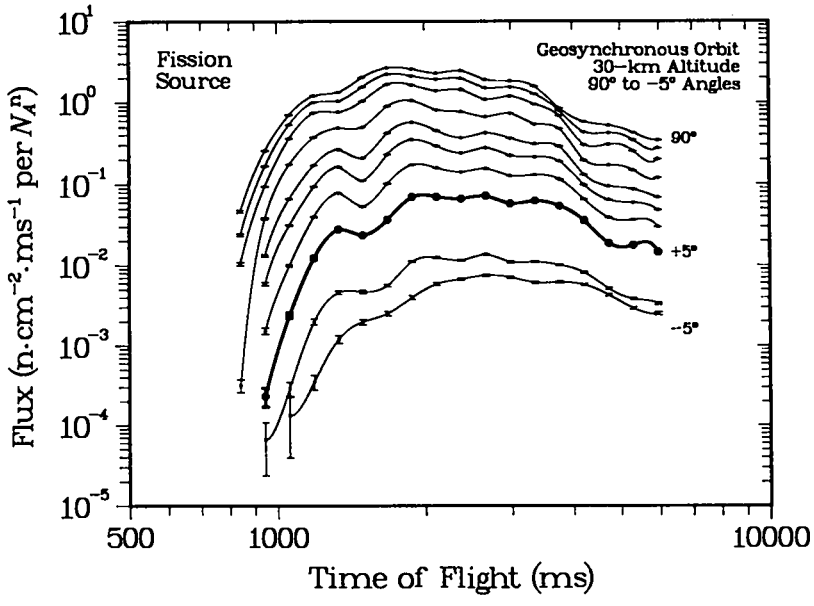

Fig. 3.13a. Summary of the angular variations in the neutron time-of-flight spectrum from a fission source at 30 km as observed at a geosynchronous detector.

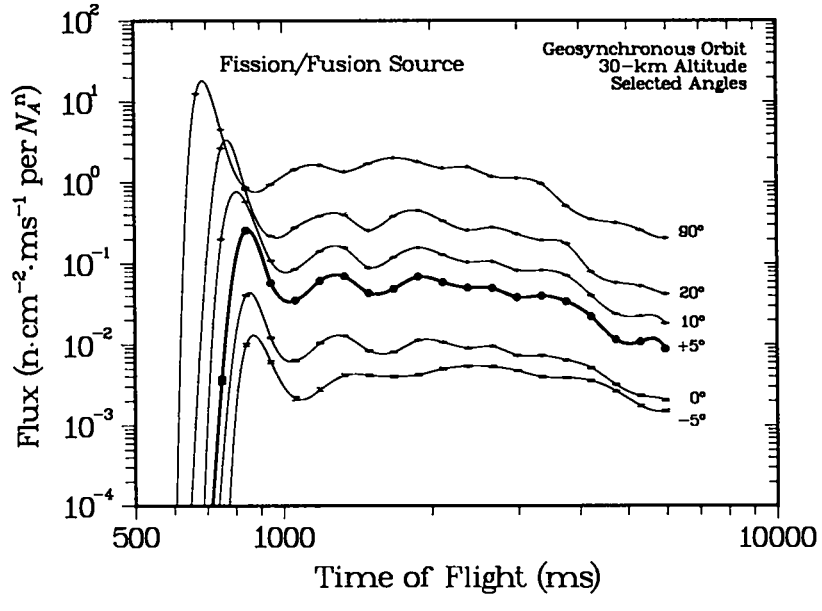

Fig. 3.13b. Collected neutron time-of-flight spectra from a fission/fusion source at 30 km as observed at a geosynchronous detector, showing selected slant angles.

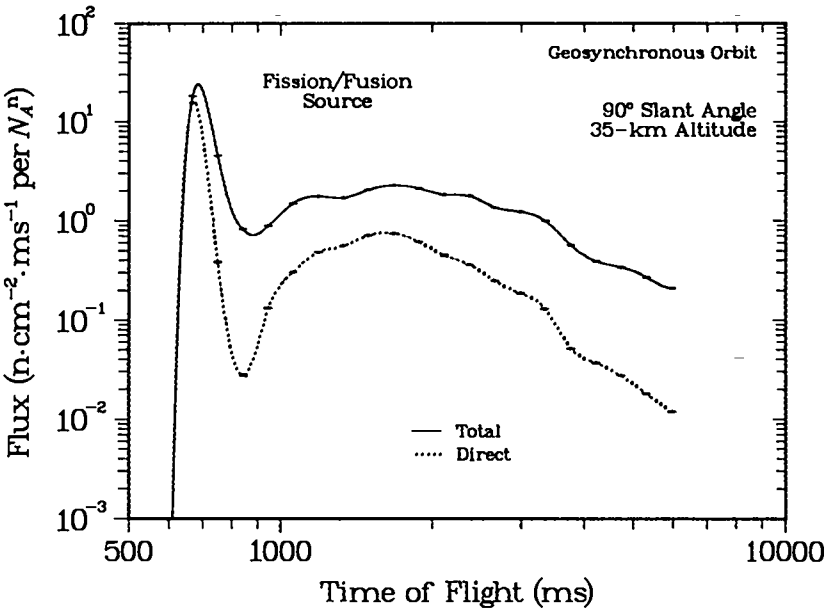

Fig. 3.14a. Total and uncollided time-of-flight spectra as observed in a geosynchronous orbit at 90° for a fission/fusion source at 35-km altitude.

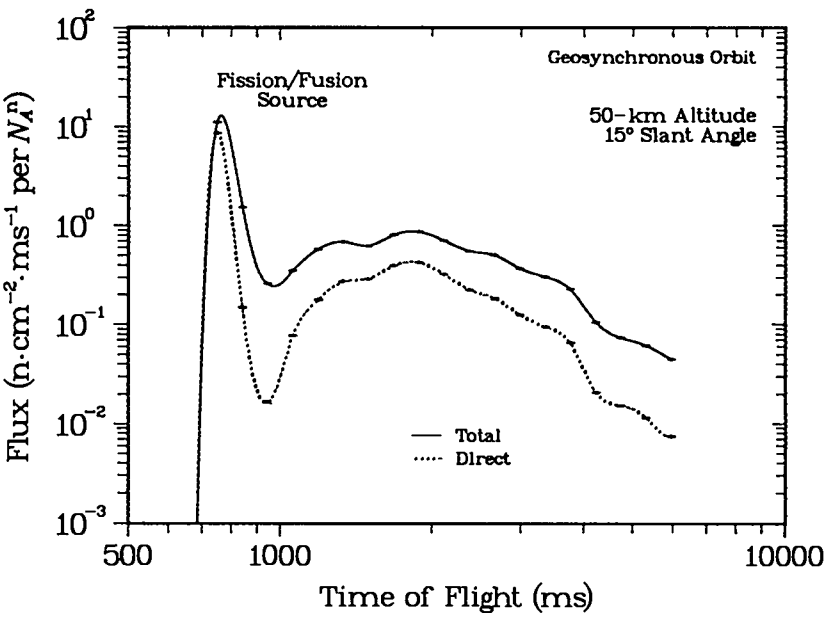

Fig. 3.14b. Total and uncollided time-of-flight spectra from a fission/fusion source at 50-km altitude as observed in a geosynchronous orbit at 15°.

these two intermediate cases (90° at 35 km, 50 km at 15°) are comparable, they have very different relationships to the free-space fluence. While the free-space and total integrals are almost identical for the 50-km case, at 35 km the observed atmospheric result is much greater in magnitude and probably very different in shape. Again, this result stresses that it is the unobservable free-space fluence, not the measured total spectrum, that has a simple connection to the original source spectrum. For neutrons, therefore, the figure of merit for interpreting the observed spectrum is not the direct-to-total ratio used in the gamma-ray case but the total transmission, which compares the observed and free-space values. Unfortunately, inspection of Figs. 3.1a,b confirms that these two quantities differ by more than 50% in all but a few cases.

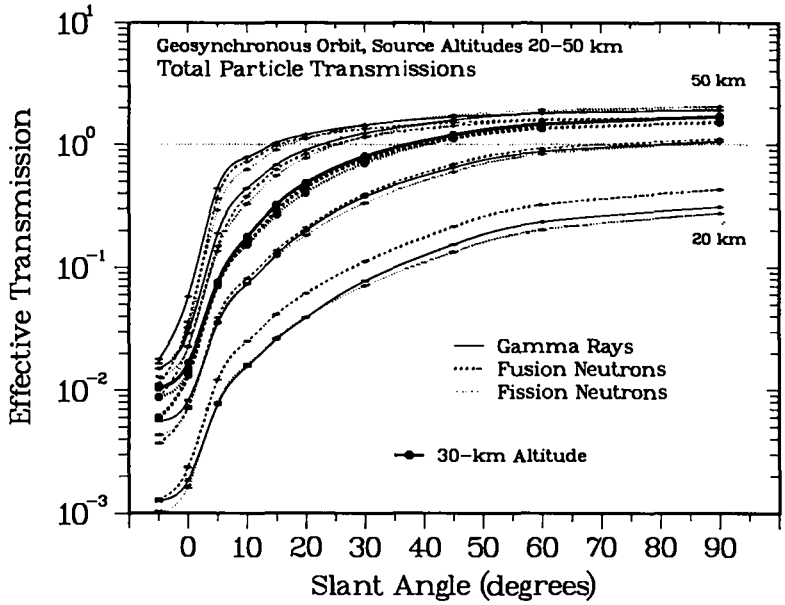

Fig. 3.15. Total transmissions for gamma rays, fusion neutrons, and fission neutrons from sources at 20- to 50-km altitudes as observed by a detector in a geosynchronous orbit.

Summary. Near the beginning of this section we pointed out the surprising similarity between the transmission results for fission and fusion sources (see Figs. 3.1a,b, for example). In fact, because the mean free paths for both neutrons and gamma rays are similar, the total particle transmissions for all three cases are almost identical, as seen in **Fig. 3.15**. Our more detailed discussions in these two sections, however, reveal that the similarity between neutron and gamma-ray particle transmissions is not as significant as it may first appear. In particular, most photon detectors respond to energy fluences, not to individual particles, and the total transmission is also less important than its direct component, which can usually be identified by its prompt arrival time at the detector. No such simplicity exists in the neutron case. Energy, not scattering, is correlated with flight time, and the low rate of absorption, that is, the much lower direct-to-total ratio, means that a large portion of the scattered fluence still reaches the detector. This scattering gives a neutron signal level that is often higher than in free space, but it also blurs

the distinctions between direct and scattered, or between fusion and fission, so that little quantitative information about the original free-space distribution is obtainable. For example, the correlation between energy and time of flight makes it easy to distinguish qualitatively between fission-only and fission/fusion sources, but it is unlikely that accurate information about a fission/fusion ratio could be obtained. As a figure of merit, in the integrated transmissions it is the ratio between the total and free-space values that is important, not the comparison of total to direct fluence. Transmissions near 1.0 should be simpler to interpret, while higher values may aid detection but indicate substantial scattering contamination; values below 0.1 may be detectable but are suitable only for qualitative analyses.

4. COUPLED NEUTRON-PHOTON CALCULATIONS

Overview. Although previous studies of atmospheric transport have covered neutron, x-ray, and delayed gamma-ray signatures, it does not appear that any calculations have been made of the production of gamma rays by neutron inelastic scattering. With the MCNP code, such studies can be made relatively easily by combining the fusion and fission sources from the neutron file with the output tallies from the gamma-ray file. In discussing the results, this section again follows the organization of the previous gamma-ray and neutron presentations, beginning with integral functions and moving on to differential energy and time spectra to provide more detailed response information.

Effective Transmissions versus Slant Angle. As in the previous gamma-ray calculations, the tally results can be presented as either particle transmissions or energy fluences. As in the neutron case, both fusion and fission sources must be considered. The particle-transmission results are shown in **Fig. 4.1a**. The y-axis label "Conversion Efficiency" refers to the relation between source neutrons and detected photons. The normalization is to the number of neutrons expected for free space, so that the efficiency compares the number of detected gamma rays produced in atmospheric reactions with the number of source neutrons that would have been observed in free space. In addition to the sharp rolloff near $+5°$, three additional features stand out: (1) the fusion and fission yields differ by more than an order of magnitude, (2) the maximum fusion transmissions approach unity (on average, each source neutron produces one detected photon), and (3) the transmission values at the highest source altitudes appear to be almost identical. The first observation, the difference between fission and fusion yields, reflects the many more inelastic-scattering channels available at higher neutron energies. The second observation, that of unity efficiency, is surprising but reasonable. For high neutron energies, (n,n′) inelastic scattering is a very likely nuclear deexcitation mode, so gamma-ray production is almost proportional to neutron inelastic scattering. Furthermore, the scattered neutron has the opportunity to undergo further reactions that produce additional gamma rays. The third feature, the similarity between different high-altitude and high-angle yields, results from two effects. First, at high source altitudes the probability of inelastic scattering (and hence gamma-ray production) has a constant value because roughly half of the source fluence is directed downward and eventually interacts with the atmosphere. Second, the probability of gamma-ray transmission to the detector is relatively constant because the energies are typically high enough that attenuation effects are small. According to this model, only at the lowest source altitudes does the attenuation become very significant.

Energy Fluences versus Angle and Altitude. For use with detector response functions, **Fig. 4.1b** provides the gamma-ray signal in absolute energy units. As in the photon transmissions, the fusion and fission responses differ by about 2 orders of magnitude, and the response falls off rapidly below the 5–10° slant angles. Compared with the

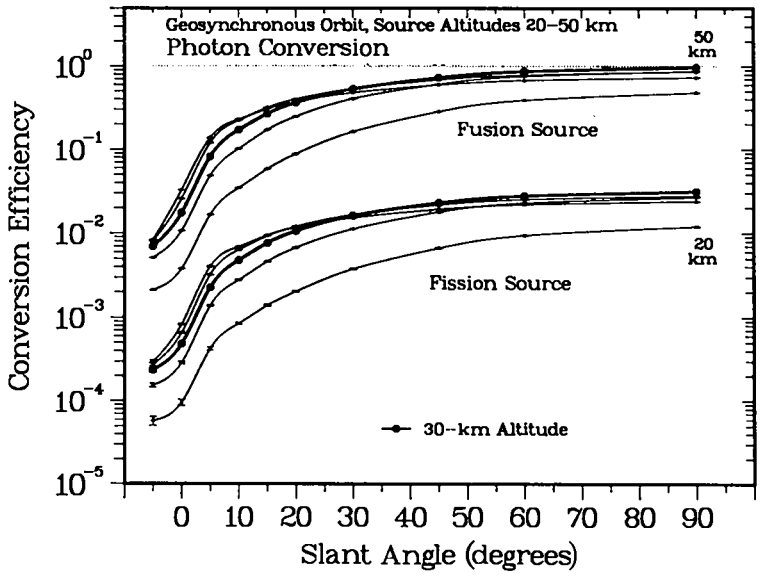

Fig. 4.1a. Conversion efficiency for neutron-photon conversion, calculated as the ratio between the observed photon flux and the expected free-space neutron fluence. The altitudes of the fission or fusion sources vary from 20 to 50 km; the detector is in a geosynchronous orbit.

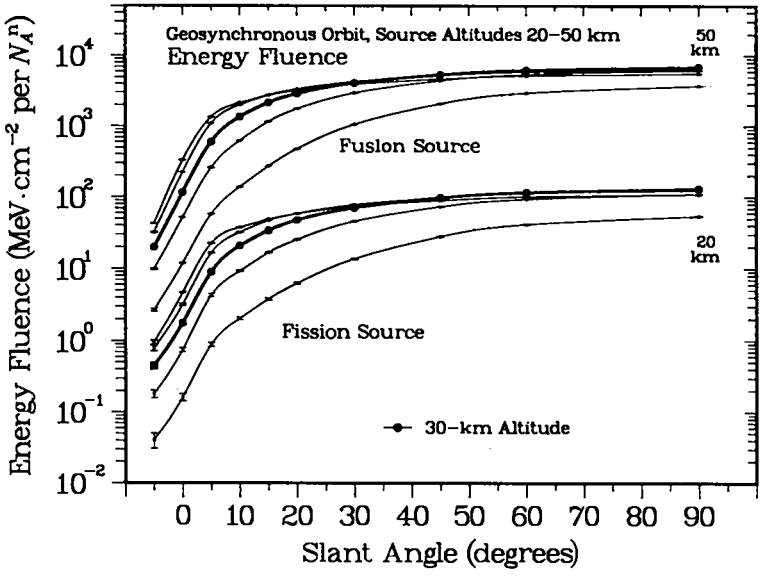

Fig. 4.1b. Slant-angle dependence of the photon energy fluence resulting from neutron-photon conversion. The altitudes of the fission or fusion sources vary from 20 to 50 km; the detector is in a geosynchronous orbit.

particle tallies, however, there is a somewhat greater falloff with source altitude, because scattered photons can lose energy but still reach the detector. This gradual falloff is seen also in **Fig. 4.1c**, which shows the altitude dependence of the energy fluence. Again, fission and fusion results are well separated, and the falloff with source altitude is slower than that with slant angle.

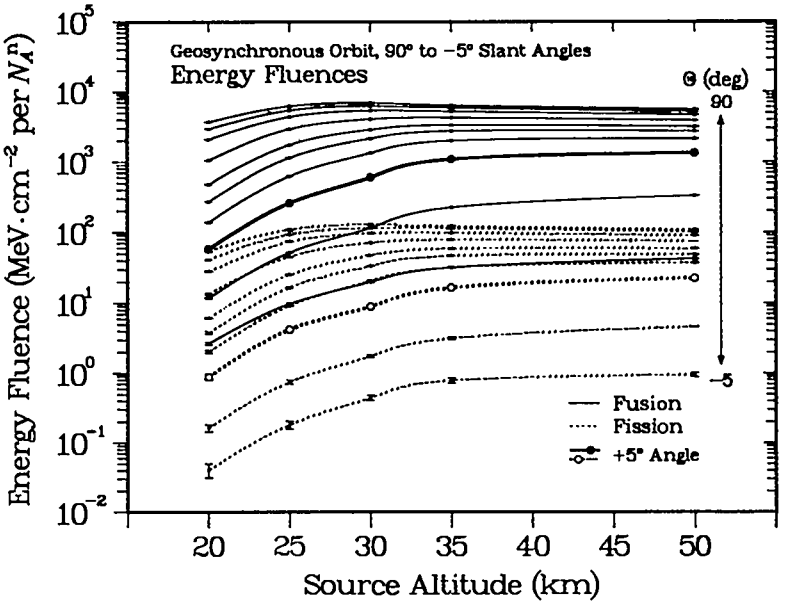

Fig. 4.1c. Altitude dependence of the photon energy fluence resulting from neutron-photon conversion of neutrons from fission or fusion sources for a detector in a geosynchronous orbit.

Differential Energy Fluences for a 30-km Source Altitude. Detectors for gamma rays from (n,n′) scattering are energy dependent, so estimates of their response require energy-dependent fluences like those shown in **Figs. 4.2a,b** for fusion and fission sources. To a large extent, the energies of the outgoing gamma rays reflect particular nuclear deexcitations, so the distinct peaks in the spectra have little to do with the incident neutron energies. This behavior is emphasized at the higher photon energies in the two figures, which differ mainly in the relative intensities of the different peaks. The spectra at the lower photon energies are dominated by downscattering and become almost featureless.

Differential Energy Fluences—Extreme Slant Angles. The 90° and +5° spectra in **Figs. 4.3a,b** provide clear examples of both the similarities and the differences between fluences at different source altitudes. In the 90° case, the near-identity of the upper-altitude distributions echoes the transmission independence discussed for Fig. 4.1a. At the +5° slant angle, the variation in yield is much greater at high than at low gamma-ray energies.

Time-Dependent Energy Fluxes—Extreme Cases. Because the neutron propagation times within the atmosphere are large compared with the subsequent photon transit time to the detector, it is not surprising that the time spectra in **Fig. 4.4** are all similar

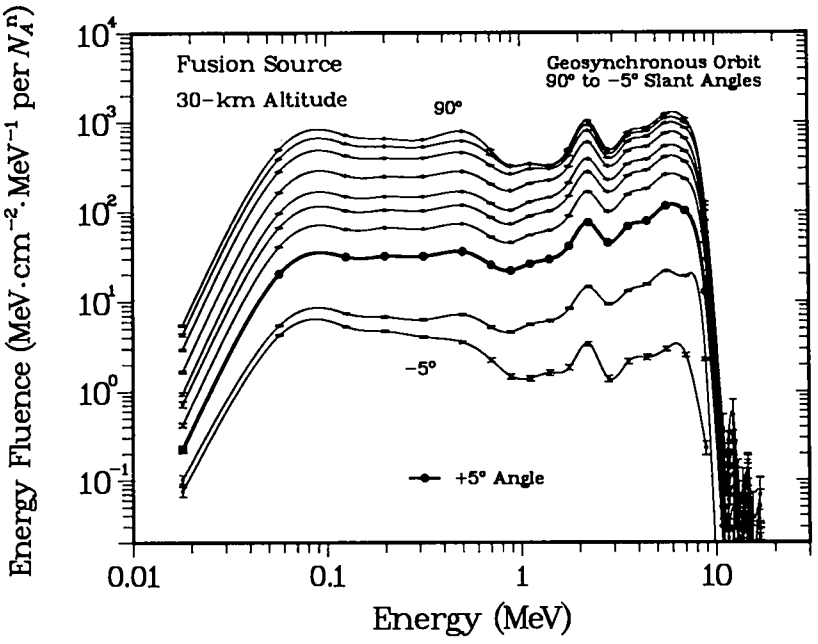

Fig. 4.2a. Angle dependence of the (n,γ) energy fluences from a fusion source at 30 km as observed in a geosynchronous orbit.

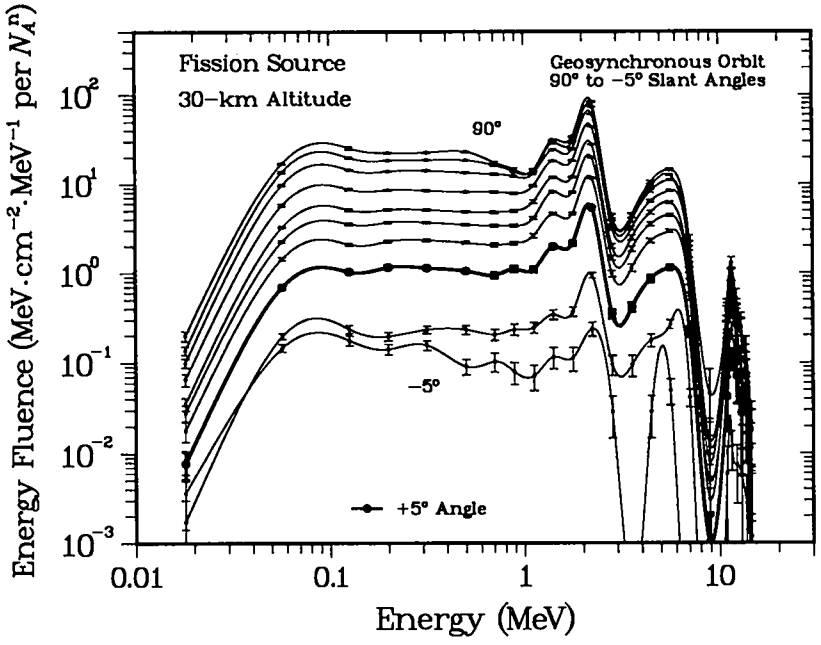

Fig. 4.2b. Energy fluences as in Fig. 4.2a, but for a fission source.

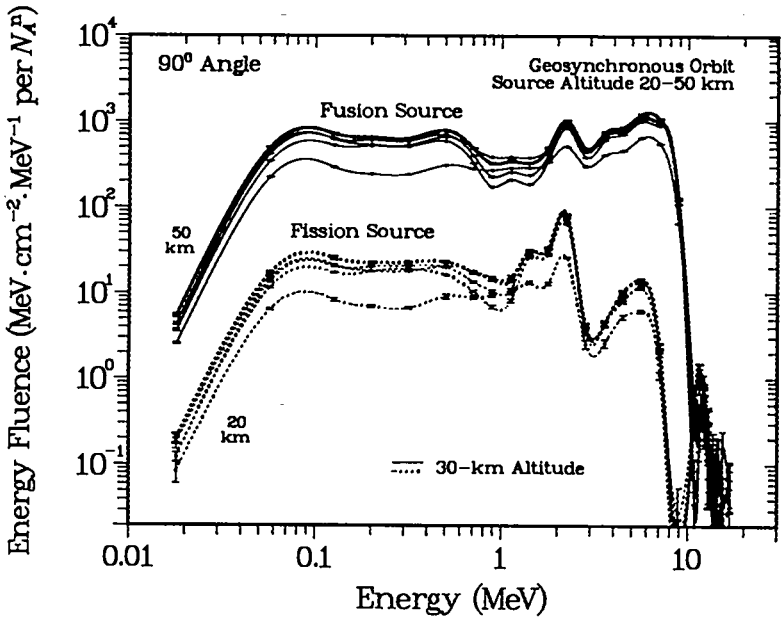

Fig. 4.3a. Altitude dependence of the (n,γ) energy fluences from fusion and fission sources at 20–50 km as observed from 90° in a geosynchronous orbit.

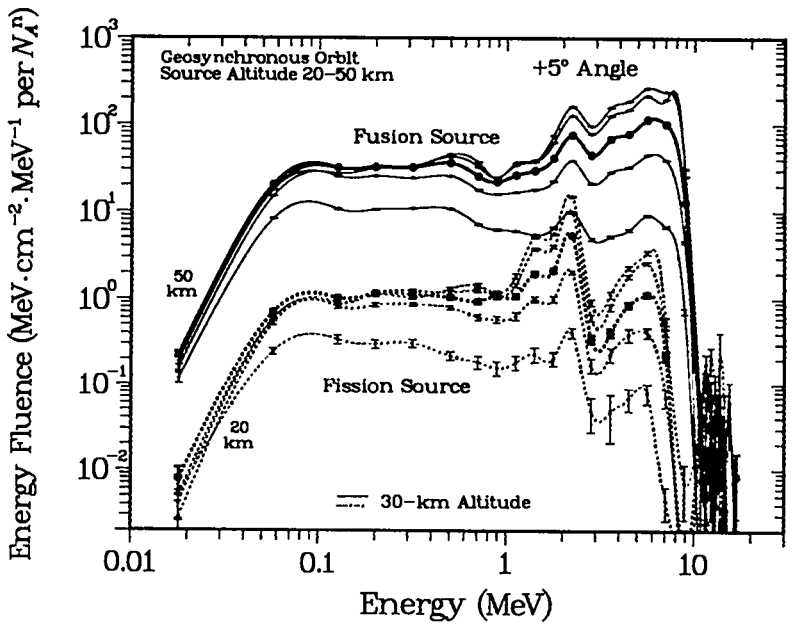

Fig. 4.3b. Energy fluences as in Fig. 4.3a, but for a +5° slant angle.

and all cover the 100- to 200-ms range of times typical of the high-energy portion of neutron time-of-flight spectra (see Figs. 3.7a,b). The solid lines show the fusion yields, whose magnitudes are greater than those for the fission sources, which are shown by the dashed lines. The light lines (with closed symbols) are for vertical angles; the heavy lines (with open symbols) are for near-horizontal angles, which appear to have a slightly different time dependence.

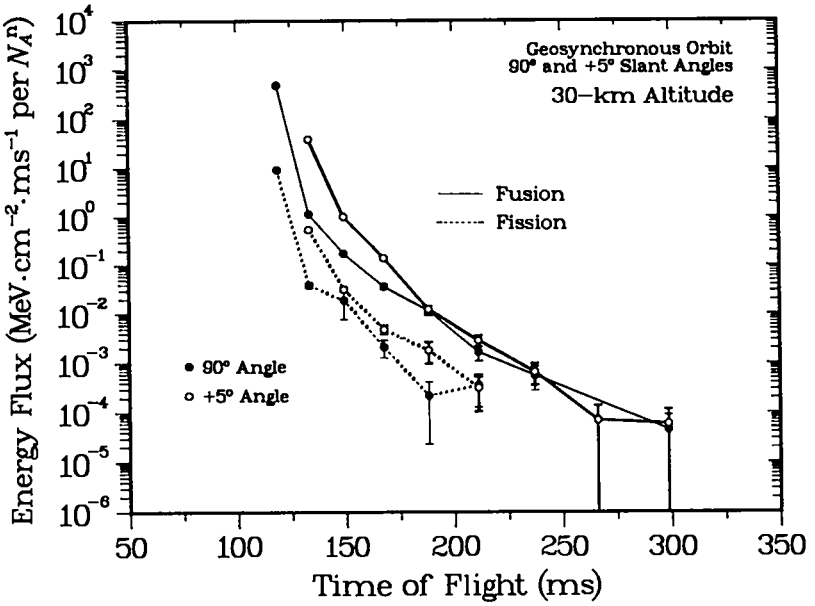

Fig. 4.4. Altitude and angle dependence of the (n,γ) energy fluxes from fusion and fission sources as observed from a geosynchronous orbit.

Summary. The major results of these first (n,n'γ) calculations are as follows. (1) Because of their higher energies, neutrons from fusion sources produce about 100 times as many gamma rays as those from fission sources. In fact, the gamma-ray production from fission sources is probably only from the highest-energy neutrons. (2) The gamma-ray production rate for fusion neutrons reaches high enough levels that on average one gamma ray is observed for every source neutron. Given that the total neutron transmissions also exceed unity, we see that fusion sources in the atmosphere can yield approximately equal numbers of detectable neutrons and inelastic-scattering gamma rays. (3) Although the intensities of the (n,n') gamma-ray fluences depend mostly on the energies of the source neutrons, the energies of the gamma rays are determined largely by atmospheric reactions and scattering and contain little source information. (4) The time dependence of the (n,n') gamma-ray fluxes roughly follows that of the high-energy neutrons and decays with a time constant of about 10 ms. This decay is slower than the 1.8-ms value for the prompt gamma rays, but it is much faster than the decay for delayed gamma-ray production from fission fragments.

5. CONCLUSIONS

Background. There have been few previous calculations for the atmospheric transport of radiation from nuclear detonations. No study has been very comprehensive in regard to different types of radiation, but all results have been generally consistent. Our focus has been on only the upper 1–5% of a near-exponential atmosphere, but we have also included low slant angles, where scattering effects are much greater. As an unclassified study, a major limitation has been the use of generic sources and unspecified detector responses. We have therefore emphasized a general understanding in terms of comparisons between transport in the atmosphere and free space, the differences between fission and fusion responses, and ratios between direct and total fluences.

Gamma-Ray Sources. The central issue in our gamma-ray discussion is the difference between the direct fluence, which contains the source information, and scattered photons, which depend mostly on transport effects. Many of our gamma-ray analyses rely on a physical model that balances the absorption of low-energy photons against the downscattering of photons from high energies. At source altitudes above 30 km and slant angles above $+5°$, the attenuation at high energies is relatively low, and the total transmitted fluence (scattered plus direct) approaches the free-space value. Over this range the rate of low-energy absorption is greater than the rate of high-energy downscattering, so the integral fluence contains mostly direct source information. In any case, most detector systems can isolate the direct component either by its early arrival time or by its higher energies. Conversely, scattered photons generally have lower energies, travel along longer paths, and arrive later, producing a characteristic atmospheric afterglow with decay times of several milliseconds. This afterglow and its associated energy dependence may be useful for identifying sources inside the atmosphere, and the direct-to-total ratios may provide a useful estimate of the source location.

Neutron Transport. All neutron analyses depend on the relationship between the measured time of flight and the actual neutron energy, a correlation that is preserved in transport through the atmosphere to the detector. The next important result is the general dominance of scattering over absorption, so that the number of neutrons remains high, but the arrival times are determined mainly by atmospheric transport, not by source characteristics. As a result, there is no way to distinguish between the scattered and direct neutron fluxes, and the total flux has no simple relation to the original source spectrum. Although it is straightforward to distinguish between the important cases of fission-plus-fusion and fission-only devices, it would be difficult to arrive at an accurate fission/fusion ratio without detailed analyses.

Inelastic (n,γ) Scattering. The major result of these calculations is the intensity of the (n,n′) gamma-ray production, which differs greatly between fission and fusion sources. In the latter cases, the photon yields average roughly one gamma ray for each source neutron—an unexpected consequence of the large amount of neutron scattering in the atmosphere. The other results should be at least qualitatively expected: the gamma-ray arrival times depend on the 10–20 ms interaction times for the high-energy part of the neutron source spectrum, and the shape of the gamma-ray energy spectrum reflects (n,n′) production on the nitrogen and oxygen components of the atmosphere, not the energies of the source neutrons. These characteristics may provide distinct signatures that allow the (n,n′) gamma-ray fluence to be distinguished from those for the prompt and delayed gamma rays.

Summary. In terms of multiple phenomenology, a unifying picture emerges from the collected set of gamma-ray and neutron calculations. The scattered gamma rays rapidly

lose energy and are absorbed, leaving a transmitted signal with reduced intensity but a direct connection to the original source, especially in its time dependence. Because neutrons tend to scatter without being absorbed, they provide a strong signal that can be uniquely distinguished from environmental effects—but this signal contains little information about device characteristics. Our preliminary work on inelastic scattering also indicates that the high energies and characteristic decay times may provide a confirmation signal but little direct source information.

Future Work. An important limitation on this study has been the need to avoid classified source and detector issues. A follow-on classified report is planned to incorporate actual neutron and gamma-ray detector responses, which would allow estimates of absolute detection thresholds. A subsequent end-to-end reanalysis based on detailed, realistic outputs for representative sources could then provide the basic information needed for a general evaluation of key system sensitivities and diagnostic capabilities.

ACKNOWLEDGMENTS

This work was supported by the Research and Technology Division of the DOE's Office of Nonproliferation and National Security. George Auchampaugh provided detailed input files from the previous calculations. The geometry for the different detector orbits and slant angles was proposed by Jerry Conner. Important discussions on the results were held with Bruce Barraclough on neutron transport, with Ed Fenimore, Fred Guyker, and Mike Meier on photon transport, and with Rick Elphic on detection issues for low-Earth orbits. Ron Chavez initiated the literature search, and George Auchampaugh and Mike Meier reviewed the final manuscript and contributed welcome suggestions for changes.

REFERENCES

1. H. W. Hubbard, "Transport Calculations Pertinent to Satellite Detection of X-Rays from Near Earth Nuclear Explosions," Rand Corporation memorandum RM-6033 (July 1, 1969) (U).
2. H. W. Hubbard, "Gamma Ray Transport Calculations," Rand Corporation unpublished figures (April 23, 1969) (U).
3. E. Fenimore, C. Ho, and B. Smith, "Simulation of Atmospheric Transmission," Los Alamos National Laboratory memorandum SST-9:92-335 (May 8, 1992) (U).
4. J. I. Marcum, "A Monte Carlo Calculation of the Neutron Time-Of-Flight Spectrum for the STARFISH Event (U)," Rand Corporation memorandum RM-5154-PR (SRD) (November 1966).
5. George Auchampaugh, "Atmospheric Neutron Leakage Spectrum from a Hypothetical Endoatmospheric Nuclear Detonation as Viewed from Space (U)," Los Alamos National Laboratory report LA-12424-MS (CRD) (September 3, 1992).
6. "U.S. Standard Atmosphere, 1976," U.S. Government Printing Office, Washington, DC 20402 (October 1976) (U).
7. W. C. Feldman et al., "Calibration of a Space Thermal/Epithermal Neutron Detector," *Nuclear Instruments and Methods* (in press) (U).
8. R. C. Byrd, G. P. Estes, and C. R. Mannon, "Far-Field Fast-Neutron Energy Spectra from an Unshielded Fission Reactor," Los Alamos National Laboratory report LA-12870-MS (March 1995) (U) .

*U.S. GOVERNMENT PRINTING OFFICE 1995-0-673-029/27000

Los Alamos
NATIONAL LABORATORY
Los Alamos, New Mexico 87545